Author/s:
Raghunathan, S;Whitehorn, N;Alvarez, MA;Aung, H;Battaglia, N;Holder, GP;Nagai, D;Pierpaoli, E;Reichardt, CL;Vieira, JD

Title:
Constraining Cluster Virialization Mechanism and Cosmology Using Thermal-SZ-selected Clusters from Future CMB Surveys

Date:
2022-02-01

Citation:
Raghunathan, S., Whitehorn, N., Alvarez, M. A., Aung, H., Battaglia, N., Holder, G. P., Nagai, D., Pierpaoli, E., Reichardt, C. L. & Vieira, J. D. (2022). Constraining Cluster Virialization Mechanism and Cosmology Using Thermal-SZ-selected Clusters from Future CMB Surveys. Astrophysical Journal, 926 (2), https://doi.org/10.3847/1538-4357/ac4712.

Persistent Link:
https://hdl.handle.net/11343/302285

The Astrophysical Journal, 926:172 (19pp), 2022 February 20 https://doi.org/10.3847/1538-4357/ac4712

Constraining Cluster Virialization Mechanism and Cosmology Using Thermal-SZ-selected Clusters from Future CMB Surveys

Srinivasan Raghunathan[1,2,3], Nathan Whitehorn[2,3], Marcelo A. Alvarez[4,5], Han Aung[6], Nicholas Battaglia[7], Gilbert P. Holder[8,9], Daisuke Nagai[6], Elena Pierpaoli[10], Christian L. Reichardt[11], and Joaquin D. Vieira[1,8,9]
[1] Center for AstroPhysical Surveys, National Center for Supercomputing Applications, Urbana, IL 61801, USA; srinirag@illinois.edu
[2] Department of Physics and Astronomy, Michigan State University, 567 Wilson Road, East Lansing, MI: 48824, USA
[3] Department of Physics and Astronomy, University of California, Los Angeles, CA 90095, USA
[4] Lawrence Berkeley National Laboratory, One Cyclotron Road, Berkeley, CA 94720, USA
[5] Berkeley Center for Cosmological Physics, UC Berkeley, CA 94720, USA
[6] Department of Physics, Yale University, New Haven, CT 06520, USA
[7] Department of Astronomy, Cornell University, Ithaca, NY 14853, USA
[8] Astronomy Department, University of Illinois at Urbana-Champaign, 1002 W. Green Street, Urbana, IL 61801, USA
[9] Department of Physics, University of Illinois Urbana-Champaign, 1110 W. Green Street, Urbana, IL 61801, USA
[10] Physics & Astronomy Department, University of Southern California, Los Angeles, CA, 90089-0484, USA
[11] School of Physics, University of Melbourne, Parkville, VIC 3010, Australia
Received 2021 July 23; revised 2021 December 26; accepted 2021 December 27; published 2022 February 22

Abstract

We forecast the number of galaxy clusters that can be detected via the thermal Sunyaev–Zel'dovich (tSZ) signals by future cosmic microwave background (CMB) experiments, primarily the wide area survey of the CMB-S4 experiment but also CMB-S4's smaller de-lensing survey and the proposed CMB-HD experiment. We predict that CMB-S4 will detect 75,000 clusters with its wide survey of $f_{\rm sky} = 50\%$ and 14,000 clusters with its deep survey of $f_{\rm sky} = 3\%$. Of these, approximately 1350 clusters will be at $z \geqslant 2$, a regime that is difficult to probe by optical or X-ray surveys. We assume CMB-HD will survey the same sky as the S4-Wide, and find that CMB-HD will detect three times more overall and an order of magnitude more $z \geqslant 2$ clusters than CMB-S4. These results include galactic and extragalactic foregrounds along with atmospheric and instrumental noise. Using CMB-cluster lensing to calibrate the cluster tSZ–mass scaling relation, we combine cluster counts with primary CMB to obtain cosmological constraints for a two-parameter extension of the standard model (ΛCDM + $\sum m_\nu + w_0$). In addition to constraining $\sigma(w_0)$ to $\lesssim$1%, we find that both surveys can enable a $\sim$2.5–4.5σ detection of $\sum m_\nu$, substantially strengthening CMB-only constraints. We also study the evolution of the intracluster medium by modeling the cluster virialization v(z) and find tight constraints from CMB-S4, with further factors of three to four improvement for CMB-HD.

Unified Astronomy Thesaurus concepts: Cosmology (343); Cosmic microwave background radiation (322); Sunyaev-Zeldovich effect (1654); Galaxy clusters (584)

1. Introduction

Galaxy clusters are the largest and most massive gravitationally bound systems in the universe. They form on the densest points of the cosmic web and hence contain a wealth of information about structure formation. Specifically, cluster abundance as a function of mass and redshift is sensitive to cosmological parameters that govern the geometry and structure growth in the universe. Of further importance is the different degeneracy directions between structure growth parameters probed by clusters compared to cosmic microwave background (CMB) or baryonic acoustic oscillations, which provide compelling joint constraints. This has been demonstrated previously in the literature (for example, Mantz et al. 2008; Vikhlinin et al. 2009; Rozo et al. 2010; von der Linden et al. 2014; de Haan et al. 2016; Salvati et al. 2018; Bocquet et al. 2019; Zubeldia & Challinor 2019; Planck Collaboration et al. 2020a), and the potential of clusters as cosmological probes from future surveys has also been a subject of extensive study (for example, Holder et al. 2001; Lima & Hu 2004; Sartoris et al. 2012; Mak & Pierpaoli 2013, and recently Louis & Alonso 2017; Madhavacheril et al. 2017; Cromer et al. 2019; Gupta et al. 2020).

Hot electrons in the intracluster medium (ICM) transfer energy to CMB photons through inverse Compton scattering (Sunyaev & Zel'dovich 1970). This thermal Sunyaev–Zeldovich effect (tSZ) has been used to detect clusters from CMB surveys (Bleem et al. 2015; Planck Collaboration et al. 2016a; Hilton et al. 2018, 2021; Huang et al. 2020; Bleem et al. 2020), and the number of clusters has been rapidly growing from a few hundreds to thousands with the increase in sensitivity of the CMB surveys (Benson et al. 2014; Henderson et al. 2016; Bender et al. 2018). Future CMB surveys like CMB-HD (Sehgal et al. 2019), CMB-S4 (CMB-S4 Collaboration 2019), Cosmic Origin Explorer (CORE; Melin et al. 2018b), and Simons Observatory (SO; Ade et al. 2019) will increase the sample size several fold, producing mass-limited cluster catalogs down to $M_{500c} \lessapprox 10^{14} M_\odot$. In the context of galaxy clusters, future CMB surveys play an important and unique role as they open the window to the high redshift $z \gtrsim 2$ universe using the redshift independent tSZ effect, enabling the detection of distant clusters. These distant clusters will otherwise be hard to detect using optical or X-ray surveys, and as a result, future tSZ-selected cluster samples will be complementary to the ones from Large Synoptic Survey Telescope (LSST) at the Vera C. Rubin

Observatory (LSST Science Collaboration et al. 2009), Euclid (Laureijs et al. 2011), and eROSITA (Merloni et al. 2012).

The clusters also gravitationally lens the background CMB, an effect known as *CMB-cluster lensing*. After the first set of detections using the CMB temperature by the Atacama Cosmology Telescope (ACT; Madhavacheril et al. 2015), South Pole Telescope (SPT; Baxter et al. 2015), and Planck (Melin & Bartlett 2015; Planck Collaboration et al. 2016b), the field has rapidly evolved to use the signal to calibrate richness–mass scaling relations of optically selected galaxy clusters (e.g., Geach & Peacock 2017) and to warrant the first polarization-only detection of the signal by SPTpol survey (Raghunathan et al. 2019b). Like the tSZ effect, CMB-cluster lensing also plays a key role in facilitating the mass measurements of distant clusters expected from future CMB surveys. This is difficult with galaxy weak lensing since the signal-to-noise ratio (S/N) of lensed background galaxies drops significantly at high redshifts. Planck Collaboration et al. (2016b) and Zubeldia & Challinor (2019) used CMB-cluster lensing information to derive cosmological constraints with the Planck cluster sample, while Alonso et al. (2016) and Madhavacheril et al. (2017) studied the potential of CMB-cluster lensing either independently or in combination with galaxy weak lensing to calibrate the observable–mass ($Y_{\rm SZ} - M$) scaling relations of clusters from CMB-S4 and its impact on cluster cosmology. While extensive studies highlighting the importance of clusters as cosmological probes exist in the literature, understanding the virialization mechanism and astrophysics of high redshift ($z \geqslant 2$) clusters mostly remains an unexplored territory owing to the lack of observations.

In this work, we focus on astrophysical and cosmological constraints using cluster samples from future CMB surveys. Our primary focus is on the wide area survey (S4-Wide) of the CMB-S4 experiment, but we also provide predictions for the smaller but deeper CMB-S4 de-lensing survey (S4-Ultra deep). The proposed CMB-HD experiment is also added to the list as an ideal case. We start by forecasting the number of tSZ-selected galaxy clusters from the three surveys. The simulations used for forecasting are designed to capture most of the effects expected in a real survey. They contain atmospheric and instrumental noise along with signals from galactic and astrophysical foregrounds. The detected clusters are then binned in lensing mass (obtained using CMB-cluster lensing), tSZ S/N q, and redshift. We combine the binned cluster counts $N(z, M_L, q)$ with primary CMB temperature and polarization spectra to derive parameter constraints. In addition to cosmology and the $Y_{\rm SZ} - M$ scaling relation, we also study the evolution of the ICM using high redshift clusters. For this, we modify the tSZ signals of clusters, using two parameterizations of the virialization model $\mathrm{v}(z) = 1 - \frac{Y_{\rm nth}}{Y_{\rm tot}}$ where $Y_{\rm th}$ and $Y_{\rm nth}$ are the thermal and nonthermal components, respectively, of the total integrated Compton-y signal $Y_{\rm tot} = Y_{\rm th} + Y_{\rm nth}$. In the first approach, we use a linear model to scale the tSZ signals from clusters with $z \geqslant 2$. We note that this toy model with a step function at $z \geqslant 2$ is over-simplistic for accurately capturing the redshift dependence of the cluster virialization process. For example, Fakhouri et al. (2010) showed that mergers, which are considered an important source of nonthermal pressure, increase as a function of redshift, which would modify the virialization mechanism of high redshift clusters. To take this into account, we build a second more realistic model using a fitting formalism, $\mathrm{v}(z) = A_{\rm v} \ln(1+z) + B_{\rm v}$, that has been derived using the analytic model of the nonthermal pressure in the ICM (Shi & Komatsu 2014; Green et al. 2020) and tested using Omega500 simulations (Nelson et al. 2014a; Shi et al. 2015).

This paper is structured as follows: We describe the simulation components, cluster virialization model, detection algorithm, mass calibration using CMB lensing, and the Fisher formalism to combine binned cluster counts with primary CMB information in Section 2. In Sections 3.1 and 3.2, we discuss the baseline results including cluster detection sensitivity, survey completeness, and cluster counts. The modification to cluster sensitivity and counts due to changes in the virialization mechanism are given in Section 3.3. We discuss the Fisher forecasts along with the impact of several choices we make in Sections 3.4 and 3.5. We test the effect of cluster correlated foreground signals in Section 3.6 and finally conclude in Section 4.

Throughout this work, we use Planck 2015 cosmology (TT+lowP in Table 4 of Planck Collaboration et al. 2016c) and report cluster masses in units of $M_{\rm 500c}$, which is the mass within a sphere of radius $R_{\rm 500c}$ where the density is 500 times the critical density of the universe at the cluster redshift.

2. Methods

2.1. Simulations

The simulations used for this study are $2^\circ \times 2^\circ$ wide CMB temperature realizations with a pixel resolution of $0\farcs5$. Other than primary CMB, the simulations also contain the following frequency-dependent signals: cluster tSZ, galactic and astrophysical foregrounds, and experimental noise (both atmospheric and instrumental). The underlying power spectrum used to generate the primary CMB is the large-scale structure lensed temperature spectrum C_ℓ^{TT} for the fiducial Planck 2015 cosmology (Planck Collaboration et al. 2016c) obtained using `CAMB` (Lewis et al. 2000) software. The cluster tSZ signal is modeled using a generalized Navarro–Frenk–White (NFW; Navarro et al. 1996; Zhao 1996; Nagai et al. 2007a; Arnaud et al. 2010) profile as described below in Section 2.4. Galactic and astrophysical foreground modelings are presented in Section 2.3. The simulated maps are then convolved by experimental beam functions, assumed to be Gaussian (see Table 1). Finally, we add noise realizations to the simulated maps. We model the noise spectra to include both atmospheric and instrumental noise as (Tegmark 1997)

$$N_\ell = \Delta_T^2 \left[1 + \left(\frac{\ell}{\ell_{\rm knee}} \right)^{-\alpha_{\rm knee}} \right], \quad (1)$$

where Δ_T^2 corresponds to detector white noise while $\ell_{\rm knee}$ and $\alpha_{\rm knee}$ are used to model the atmospheric $1/f$ noise. This parameterization gives us a sense of the range of multipoles being affected by the atmospheric ($\ell < \ell_{\rm knee}$) and instrumental noise components ($\ell \geqslant \ell_{\rm knee}$).

2.2. Experimental Setup

We consider three future CMB surveys in this work: CMB-HD, S4-Wide, and S4-Ultra deep. Table 1 lists the instrumental noise levels Δ_T (μK − arcmin) and experimental beams of each frequency band for the three surveys. CMB-HD is a proposed high-resolution millimeter-wave survey scanning large regions of the sky from Chile with a 30 m primary mirror and designed to operate in seven bands from 30–350 GHz (Sehgal et al. 2019, 2020). CMB-S4 is an upcoming survey that is currently

Table 1
Experimental Specifications

Experiment	Location ($f_{\rm sky}$)	Beam $\theta_{\rm FWHM}$ [arcminutes]							Δ_T [μK − arcmin]						
		30	40	90	150	220	270	350	30	40	90	150	220	270	350
CMB-HD	Chile (67%)	1.4	1.05	0.45	0.25	0.20	0.15	0.12	6.5	3.4	0.73	0.79	2.0	2.7	100
S4-Wide		7.3	5.5	2.3	1.5	1.0	0.8	…	21.8	12.4	2.0	2.0	6.9	16.7	…
S4-Ultra deep	South Pole (3%)	8.4	5.8	2.5	1.6	1.1	1.0	…	4.6	2.94	0.45	0.41	1.29	3.07	…

in its design stages and expected to start operations later this decade (CMB-S4 Collaboration 2019). In this work, we only consider the two CMB-S4 large aperture telescope surveys and not the small aperture telescope survey that is aimed at the inflationary gravitational waves. The two S4-LAT surveys (S4-Wide and S4-Ultra deep) will be performed using 6 m class telescopes in six[12] frequency bands from 30 to 270 GHz. S4-Wide is a legacy survey from Chile and will cover roughly 67% of the sky area. S4-Ultra deep is the "de-lensing" survey that is aiming to provide deep observations of ∼3% of the sky from the South Pole. The primary objective of the S4-Ultra deep survey is to generate high-resolution maps of the dark matter distribution in the universe to facilitate the detection of inflationary B-modes by cleaning the lensing-induced B-modes. However, given the large telescope size, S4-Ultra deep also has the capability to detect high redshift SZ clusters, as we show in this work. The parameters governing the atmospheric $1/f$ noise, $\ell_{\rm knee}$ and $\alpha_{\rm knee}$, are listed in Table 2 (CMB-S4 Collaboration 2019). For simplicity, we assume the $1/f$ model and sky fraction for CMB-HD to be the same as those in the Chile-based S4-Wide survey.

2.3. Foreground Signals

Although extragalactic foregrounds, emissions from dusty star-forming galaxies (DSFGs) in particular, are expected to be the major source of contamination for cluster detection, the footprint of Chile-based experiments cover 67% of the sky area and will be subjected to contamination from galactic emission. Hence, we consider both galactic and extragalactic foreground signals for CMB-HD and S4-Wide. For S4-Ultra deep, we only include extragalactic foregrounds, as it will observe a relatively clean region of the sky shown as the yellow dashed contours in Figure 1.

2.3.1. Galactic Emission

The galactic foreground signals, dust and synchrotron, are position dependent and hence one cannot rely on Gaussian realizations of an underlying power spectrum for the entire footprint. To this end, we use the publicly available pySM3 dust and synchrotron map simulations,[13] which were built specifically in the context of CMB-S4. For more details about pySM3 simulations, we refer the reader to the original work (Thorne et al. 2017), which is partly based on the Planck Sky Model code (Delabrouille et al. 2013). We use `S0_d0` dust and `S0_s0` synchrotron models of pySM where the dust temperature, dust emissivity index, and synchrotron spectral index do not have spatial variations. The models also ignore any non-Gaussianities. Other galactic signals like free–free and anomalous microwave emissions, which should have a negligible impact on cluster searches, are ignored in this work. To estimate the position-dependent galactic foregrounds, we first divide the S4-Wide footprint into two *high* and *low* emission regions, shown as the red and blue contours in Figure 1. The high emission region corresponds to $\pm 15^\circ$ and encompasses most of the signals from the galactic plane. The low emission region corresponds to regions in the range $-45^\circ \leqslant b \leqslant -30^\circ$. We compute the temperature power spectra $C_\ell^{\rm gal}$ of dust and synchrotron signals of both these regions for all of the frequency bands of interest.

We assume 23% ($f_{\rm sky} = 17\%$) of the S4-Wide footprint to have galactic signals similar to the high emission region and the galactic signals in the remaining 77% ($f_{\rm sky} = 50\%$) to be similar to the low emission region. As is evident from the figure, the blue contours do not correspond to the cleanest region in the S4-Wide footprint, and hence this is a conservative choice. With this assumption, we use the $C_\ell^{\rm gal}$ spectra estimated in the two regions to generate Gaussian realizations of galactic emission and add them to our maps to produce two sets of simulated skies. The underlying power spectrum for the other signals in the two sets is the same. By doing this, we approximate the galactic power spectra to be constant inside the two regions. We validated this assumption by dividing the S4-Wide footprint into six regions (latitude steps of $\Delta b = 15^\circ$) with different galactic emission and do not find a significant difference in the number of detected clusters between the two approaches. We follow the same approach for CMB-HD. Like mentioned above, since the footprint of S4-Ultra deep lies in a relatively clean region, we do not include galactic foregrounds for S4-Ultra deep simulations.

The CMB-S4 pySM3 simulations do not include the 350 GHz band, which is required for CMB-HD. We obtain auto-spectra of the galactic dust at the 350 GHz band and its cross correlation with other bands by simply scaling the

Table 2
Atmospheric $1/f$ Noise Specifications ($\ell_{\rm knee}$, $\alpha_{\rm knee}$)

Band [GHz]	CMB-HD	S4-Wide	S4-Ultra deep
30	471, 3.5		1200, 4.2
40	478, 3.5		1200, 4.2
90	2154, 3.5		1200, 4.2
150	4364, 3.5		1900, 4.1
220	7334, 3.5		2100, 3.9
270	7308, 3.5		2100, 3.9
350	7500, 3.5	…	…

[12] S4-Ultra deep is also expected to have a 20 GHz band, but we ignore that in this work for simplicity.
[13] https://github.com/CMB-S4/s4mapbasedsims/tree/master/202102_design_tool_input

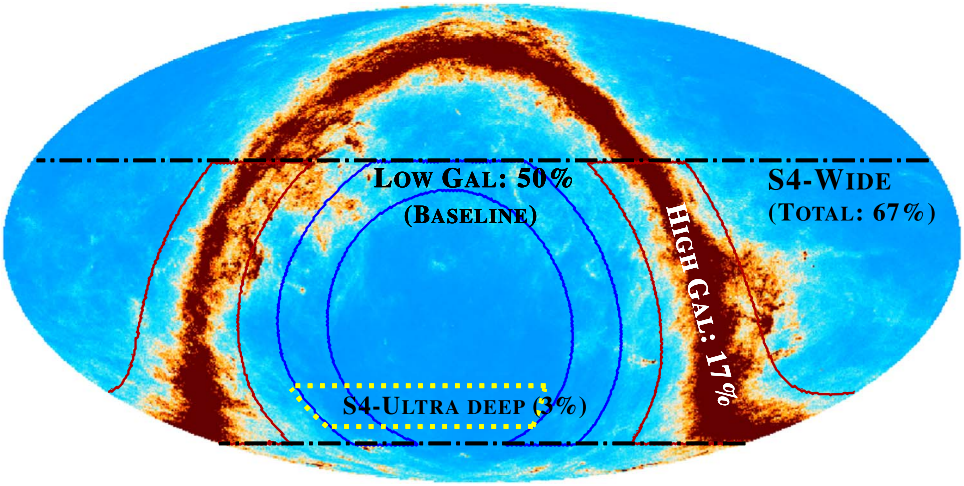

Figure 1. Map of the galactic dust emission at 150 GHz from pySM3 simulations. The expected footprints for S4-Wide ($f_{\rm sky} = 67\%$) and S4-Ultra deep ($f_{\rm sky} = 3\%$) are highlighted in black and yellow. Regions of high and low galactic emissions used for injecting galactic foregrounds in our simulations are marked as red and blue contours. We assume the galactic emission in 23% of the S4-Wide footprint ($f_{\rm sky} = 17\%$) to be similar to high galactic emission in the red contours and the emission in the remaining 77% ($f_{\rm sky} = 50\%$) to be similar to low galactic emission in the blue contours (marked as baseline). This is a conservative choice as the blue contours are not the cleanest region in the S4-Wide footprint. We use the same S4-Wide footprint and strategy for CMB-HD. Since S4-Ultra deep will observe in a relatively clean patch, we do not include galactic foregrounds for S4-Ultra deep simulations.

270 GHz dust spectra as

$$C^{\rm gal-dust}_{\ell,\nu_1\nu_2} = C_{\ell,\nu_0\nu_0}\ \epsilon_{\nu_1,\nu_2}\ \frac{\eta_{\nu_1}\eta_{\nu_2}}{\eta_{\nu_0}\eta_{\nu_0}}, \quad (2)$$

where $\nu_0 = 270$ GHz and ν_1, $\nu_2 \in$[30, 40, 90, 150, 220, 270, 353] GHz. The terms ϵ_ν and η_ν in Equation (2) when combined represent the spectral energy distribution (f_ν, SED) of dust, and we use a modified blackbody of the form

$$\eta_\nu = \nu^{\beta_d}\ B_\nu(T_d), \quad (3)$$

and

$$\epsilon_{\nu_1,\nu_2} = \left.\frac{\frac{dB_{\nu_0}}{dT}\frac{dB_{\nu_0}}{dT}}{\frac{dB_{\nu_1}}{dT}\frac{dB_{\nu_2}}{dT}}\right|_{T=T_{\rm CMB}}. \quad (4)$$

$B_\nu(T)$ in the above equations is the Planck function, and we set $T_{\rm CMB} = 2.73$ K, emissivity index $\beta_d = 1.6$, and dust temperature $T_d = 19.6$ K, similar to pySM3 simulations that are consistent with measurements from Planck (Planck Collaboration et al. 2020b). We ignore synchrotron signals at 350 GHz since they are expected to be negligible compared to dust at such high frequencies.

2.3.2. Extragalactic Foregrounds

Diffuse extragalactic foreground signal can be decomposed into: emissions from DSFGs and radio galaxies (RGs) below the detection threshold; and kinetic SZ (kSZ) and tSZ signals. Note that DSFGs are responsible for cosmic infrared background (CIB) anisotropies at millimeter/submillimeter wavelengths, and we sometimes use the two terms, DSFGs and CIB, interchangeably in this work. DSFG and RG signals were all modeled as Gaussian realizations using SPT power spectra measurements (George et al. 2015; Reichardt et al. 2021). SPT observations masked DSFGs and RGs detected above 5σ, which corresponds to a flux threshold of $S_{150} \sim 6$ mJy. However, the 5σ detection limit for the future surveys considered here will be much lower: $S_{150} \sim 2$ mJy for CMB-S4 (CMB-S4 Collaboration 2019) and $\leqslant 0.1$ mJy for CMB-HD (Sehgal et al. 2019). For CMB-S4, we do not modify the masking threshold and simply use SPT measurements. Thus, DSFG and RG signals injected into S4-Wide and S4-Ultra deep simulations are conservative estimates. For CMB-HD, however, Sehgal et al. (2019) claim that sources with flux above $S_{150} \geqslant 0.04$ mJy can be efficiently removed by detecting them at $\geqslant 3\sigma$ in the 270/350 GHz bands. This lowers the DSFG power in 150 GHz by $\times 17$, and we adopt that strategy here. The masking threshold for RG is not modified from SPT values. The frequency dependence of DSFG and RG signals is also adopted from SPT (George et al. 2015; Reichardt et al. 2021) measurements. We introduce decorrelation in the DSFG signals between the 270/350 GHz and 150 GHz bands using SPT $\times$ Herschel/Spectral and Photometric Imaging Receiver (SPIRE) measurements (Viero et al. 2019). We estimate the correlation coefficient between the 150 GHz and 270/350 GHz bands by interpolating the values in Table 1 of Viero et al. (2019).

The kSZ signal is contributed to by two distinct sources: one from the Doppler boosting of CMB photons due to the motion of haloes and the other from the epoch of reionization. We use the Reichardt et al. (2021) measurement to simulate the kSZ signal. This roughly corresponds to flat spectrum in D_ℓ with $D_{\ell,3000} = 3\ \mu{\rm K}^2$ where $D_\ell = C_\ell\ \frac{\ell(\ell+1)}{2\pi}$ and has no frequency dependence. For the diffuse tSZ, we consider power from all haloes with $M_{500c} \geqslant 10^{13}\ M_\odot$, modeled using the Arnaud profile (Arnaud et al. 2010), in the redshift range $z \in [0.1, 4.0]$. Both the diffuse kSZ and tSZ signals are simulated as Gaussian realizations using the respective power spectra described above.

In our fiducial setup, DSFG/RG/kSZ signals are assumed to be uncorrelated to the cluster under study. This is, however, not entirely correct as galaxies preferentially reside inside clusters, and the cluster motion can also give rise to kSZ signals. We test this assumption in Section 3.6 by injecting cluster correlated foreground signals using Websky (Stein et al. 2020) and MultiDark Planck 2 (MDPL2, Y. Omori 2022, in preparation) simulations.

2.4. Cluster tSZ Signal

We model the ICM pressure using the dimensionless universal pressure profile $P_e(x)$ proposed by Nagai et al. (2007a) and calibrated using X-ray observations by Arnaud et al. (2010)

$$P_e(l, x) = \frac{P_0}{(c_{500}x)^{\gamma}[1 + (c_{500}x)^{\alpha}]^{(\frac{\beta-\gamma}{\alpha})}}, \quad (5)$$

where the distance to the cluster center $x \equiv xR_{500}$, expressed in terms of virial radius R_{500}, and concentration parameter c_{500} are related to scale radius r_s as $x = r/r_s$ and $c_{500} = R_{500}/r_s$. The best-fit values of the parameters are (Arnaud et al. 2010): $c_{500} = 1.177$, the normalization constant $P_0 = 8.403\ h_{70}^{-3/2}$, and the exponents are $\alpha = 1.0510$, $\beta = 5.4905$, and $\gamma = 0.3081$. The pressure profile $P_e(l, x)$ is integrated along the line of sight to obtain the Compton-y signal $y(x)$ as

$$y(x) = \frac{\sigma_T}{m_e c^2} \int_l P_e(l, x)\, dl \quad (6)$$

and is converted into CMB temperature units as

$$\delta_T = y(x)\ g_{\rm SZ}(\nu) T_{\rm CMB}\ {\rm K}, \quad (7)$$

where σ_T in the Thomson cross section, c is the velocity of light, m_e is the electron mass, $T_{\rm CMB} = 2.73$ K is the mean temperature of the CMB, and $g_{\rm SZ}(\nu)$ is the frequency dependence of the tSZ signal, which, ignoring relativistic SZ corrections (e.g., Itoh et al. 1998; Chluba et al. 2012), is given by

$$g_{\rm SZ}(\nu) = x\ \coth(x/2) - 4;\ x = \frac{h\nu}{k_B T_{\rm CMB}}, \quad (8)$$

where h and k_B are Planck and Boltzmann constants, respectively.

We integrate $y(x)$ over the angular extent of the cluster R_{500} to obtain the total integrated cluster Compton $Y_{{\rm SZ}_{500c}}$ defined using Planck Collaboration et al. (2016b) but generalized based on Alonso et al. (2016) and Madhavacheril et al. (2017) to include mass and redshift evolution as

$$Y_{{\rm SZ}_{500c}} = v(z)\ Y_* \left[\frac{h}{0.7}\right]^{-2+\alpha_Y} \left[\frac{M_{\rm 500c}}{M_*}\right]^{\alpha_Y} e^{\beta_Y \log^2\left(\frac{M_{\rm 500c}}{M_*}\right)} \left[\frac{D_A(z)}{100\ {\rm Mpc}}\right]^2 E^{2/3}(z)\ (1+z)^{\gamma_Y}, \quad (9)$$

where $M_* = 6 \times 10^{14} M_\odot$ is the pivotal mass, $D_A(z)$ is the angular diameter distance to the cluster at redshift z, $E(z) = H(z)/H_0$ is the Hubble function, and $M_{\rm 500c}$ is the mass of the cluster. v(z) in the above equation is the cluster virialization model adopted to modify the cluster tSZ signal and is explained below in Section 2.5. We use Planck Collaboration et al. (2016b) best-fit values to fix $\log Y_* = -0.19$ and $\alpha_Y = 1.79$. The fiducial values for redshift γ_Y and second-order mass β_Y evolution parameters are set to zero. The log-normal scatter $\sigma_{\log Y_{{\rm SZ}_{500c}}} \equiv \sigma_{\log Y}$ in the above relation is modeled similar to that in Madhavacheril et al. (2017) to include mass and redshift evolution as

$$\sigma_{\log Y}(M_{\rm 500c}, z) = \sigma_{\log Y,0} \left[\frac{M_{\rm 500c}}{M_*}\right]^{\alpha_\sigma} (1+z)^{\gamma_\sigma} \quad (10)$$

with the fiducial values set to $\sigma_{\log Y,0} = 0.127$, $\alpha_\sigma = 0$, and $\gamma_\sigma = 0$ (Louis & Alonso 2017).

2.5. Modeling the Cluster Virialization

Not much is known about the astrophysics of high redshift clusters owing to the lack of sufficient observations. Lately, Mantz et al. (2014) and Mantz et al. (2018) used Combined Array for Research in Millimeter-wave Astronomy (CARMA) data to perform detailed tSZ study of a distant cluster at $z = 1.99^{+0.19}_{-0.21}$ with $M_{\rm 500c} \sim 1 - 2 \times 10^{14} M_\odot$ that was detected by the X-ray XMM-Newton satellite. Mantz et al. (2018) report that the properties of this distant cluster are in reasonable agreement with the extrapolated scaling relations confirming self-similar evolution of clusters out to $z \sim 2$. However, the authors also caution the readers about generalizing the result from a single $z \sim 2$ cluster to all high redshift clusters. As we will see later in Section 3.2, CMB-HD and CMB-S4 have the capability to detect hundreds to thousands of clusters with $M_{\rm 500c} \lesssim 10^{14}\, M_\odot$ at $z \gtrsim 2$. Subsequently, we aim to study the physics of the ICM and its evolution out to high redshifts with these potential detections. To this end, we tweak the first term in Equation (9), $v(z) \equiv \left[1 - \frac{Y_{\rm non-th}}{Y_{\rm tot}}\right]$ that controls cluster virialization and as a result modifies the cluster tSZ signal. We model $v(z)$ in two different ways as described below.

2.5.1. Linear Scaling: Model 1

In the first approach, we use a simple model

$${\rm v}(z) = \eta_{\rm v}(z)\ (1 - b_{\rm HSE})^{\alpha_Y}, \quad (11)$$

where $b_{\rm HSE}$ is the hydrostatic equilibrium (HSE) mass bias set to $b_{\rm HSE} = 0.2$ (Zubeldia & Challinor 2019; Makiya et al. 2020) and assumed to be constant for clusters at all redshifts. $\eta_{\rm v}(z)$ is the *virialization efficiency* of clusters that modifies the tSZ signal of clusters using a linear scaling as

$$\eta_{\rm v}(z) = \begin{cases} 1, z < 2 \\ 1 + \epsilon, z \geqslant 2 \end{cases} \quad (12)$$

with $\epsilon \in [-1, 1]$. This model is similar to the $Y_{\rm SZ} - M$ relation used in Planck Collaboration et al. (2016b) except for the introduction of $\eta_{\rm v}(z)$ for high-z clusters. The fiducial value of $\eta_{\rm v}(z) = 1$ for all clusters.

2.5.2. Physically Motivated Model 2

Since the step function at $z \geqslant 2$ used in the above model is highly simplistic, we now build a realistic model to parameterize the redshift dependence of the virialization process (e.g., Fakhouri et al. 2010) more accurately. In this second approach, we use the analytic model for modeling the evolution of the nonthermal pressure fraction through the cluster assembly and virialization processes (Shi et al. 2015) and their impact on the $Y_{\rm SZ} - M$ relation of high redshift clusters using the model presented in Green et al. (2020). We summarize the modeling and results in the Appendix, in which

we use a fitting formalism

$$\mathrm{v}(z) = A_\mathrm{v} \ln(1+z) + B_\mathrm{v} \tag{13}$$

derived from the analytical model of nonthermal pressure (Shi & Komatsu 2014; Green et al. 2020) and tested using the Omega500 hydrodynamical cosmological simulation (Nelson et al. 2014a; Shi et al. 2015). We set the fiducial values of the parameters to be $A_\mathrm{v} = 0.155$ and $B_\mathrm{v} = 0.189$.

2.6. Cluster Detection

We combine the simulated maps in different frequency channels N_ch optimally using an internal linear combination (ILC) algorithm and create a Compton-y map as

$$y_\ell = \sum_{i=1}^{\mathrm{N}_{ch}} w_\ell^i M_\ell^i, \tag{14}$$

where the multipole-dependent weights w_ℓ for each frequency channel are computed using the SMICA (Spectral Matching Independent Component Analysis) algorithm (Cardoso et al. 2008; Remazeilles et al. 2011; Planck Collaboration et al. 2014) as

$$w_\ell = \frac{\boldsymbol{C}_\ell^{-1}\boldsymbol{a}}{\boldsymbol{a}^T\boldsymbol{C}_\ell^{-1}\boldsymbol{a}}. \tag{15}$$

The matrix $\mathbf{C}_\ell$ has a dimension $\mathrm{N}_{ch} \times \mathrm{N}_{ch}$ and contains the covariance between simulated maps in multiple frequencies at a given multipole ℓ. The frequency response vector $\boldsymbol{a} = [-5.33, -5.23, -4.36, -2.61, 0.09, 2.27, 5.95]$ contains the tSZ spectrum given in Equation (8) for [30, 40, 90, 150, 220, 270, 350] GHz channels. The weights in Equation (15) for each band are chosen optimally to produce a minimum variance Compton-y map by jointly minimizing the contamination from the noise and foreground signals that are uncorrelated with the cluster. We do not explicitly null any foreground components using a constrained ILC technique (Remazeilles et al. 2011), but study the effect of cluster correlated foreground signals in Section 3.6.

2.6.1. Maximum Likelihood Approach

The resultant ILC Compton-y map is then used to compute the S/N of the cluster tSZ signal using a maximum likelihood–based approach. For blind cluster searches, however, adopting a multiband matched-filtering technique (Melin et al. 2006) would be computationally more feasible as done traditionally in cluster finding using CMB surveys (e.g., Bleem et al. 2015). The two approaches are equivalent. In addition to the cluster tSZ signal, this map includes variance from diffuse tSZ and also the residual CMB, foreground signals, and noise. Using this $2^\circ \times 2^\circ$ ILC y map, we calculate

$$-2\ln\mathcal{L} = \sum_{ij} (\hat{\boldsymbol{y}}_i - \boldsymbol{y}_i^{\mathrm{th}}) \hat{C}_{ij}^{-1} (\hat{\boldsymbol{y}}_j - \boldsymbol{y}_j^{\mathrm{th}}), \tag{16}$$

where $\boldsymbol{y}_i \equiv \boldsymbol{y}_i(\theta)$ is the azimuthally averaged profile of the Compton-y signal in bins i of $\Delta\theta = 0.''5$, out to a maximum $\theta_\mathrm{max} = 2'$. The chosen θ_max encompasses the tSZ signal from the majority of the clusters at all redshifts and hence maximizes the S/N. Specifically, $\theta_\mathrm{max} \geqslant \theta_{500c}$ for clusters with $z \gtrsim 0.5$ where $\theta_{500c} = R_{500c}/D_A(z)$ and $D_A(z)$. The measured cluster Compton-y from a cluster with a given mass and redshift is $\hat{\boldsymbol{y}}$. We compute theory models $\boldsymbol{y}$th for different masses at the cluster redshift using Equation (9) and fit them to the measured $\hat{\boldsymbol{y}}$ signal. The covariance matrix $\hat{C}$ includes contribution from other sources of variance described above. It is computed using $N = 2500$ simulations as

$$\hat{C} = \frac{1}{N-1}\sum_{n=1}^{N} (\hat{\boldsymbol{y}}_i - \langle\hat{\boldsymbol{y}}\rangle)(\hat{\boldsymbol{y}}_i - \langle\hat{\boldsymbol{y}}\rangle)^T. \tag{17}$$

We use the distribution of best fits recovered from 100 simulations and compute the S/N as the inverse of the 1σ uncertainty defined by the 16% to 84% confidence range. For each survey, we compute an S/N look-up table in this way for different clusters in an (M_{500c}, z) grid: $\log M_{500c} \in [13, 15.4]\ M_\odot$ with $\log \Delta M = 0.1\ M_\odot$ and $z \in [0.1, 3]$ with $\Delta z = 0.1$. This S/N look-up table is used to select clusters above the detection threshold $\mathrm{S/N} \equiv q = 5$ in later sections.

2.7. Mass Calibration Using CMB Lensing

We perform internal mass calibration of clusters using their gravitational lensing signatures on both CMB temperature and polarization anisotropies. Cluster kSZ and tSZ signals are expected to introduce significant bias to temperature-based lensing reconstruction (Raghunathan et al. 2017). We mitigate them by employing an inpainted-gradient (Raghunathan et al. 2019a) quadratic temperature lensing estimator (QE; Hu et al. 2007). This estimator reconstructs lensing using the lensing-induced correlations between a large-scale and a small-scale temperature anisotropies map. Cluster SZ signals, in addition to lensing, can also introduce such correlations, which tend to bias best-fit lensing masses. In the inpainted-gradient QE, we remove SZ signals in the large-scale gradient map by estimating the pixel values at the cluster location using information from adjacent pixels. For polarization, we use the optimal maximum likelihood estimator (MLE; Raghunathan et al. 2017), which reconstructs cluster masses using the lensing-induced changes to a pixel-pixel covariance matrix. We ignore the covariance between temperature and polarization but note that it can slightly degrade the lensing S/N.

2.8. Fisher Formalism

We use the Fisher matrix formalism (Holder et al. 2001) and compute

$$F_{\theta_i\theta_j} = \sum_{z,M_L,q} \frac{\partial N(z, M_L, q)}{\partial\theta_i} \frac{\partial N(z, M_L, q)}{\partial\theta_j} \frac{1}{N(z, M_L, q)}, \tag{18}$$

where θ_i, θ_j are the astrophysical or cosmological parameters to be constrained; $N(z, M_L, q)$ is the number of clusters in a given lensing mass M_L, tSZ S/N q, and redshift z bin; and $1/N(z, M_L, q)$ gives the Poisson error in each bin. The summation indices lqz run over the M_L, q, and z bins described below in Section 2.8.2. Cluster number counts in a given bin $N(z_i, M_{L_j}, q_k) \equiv N(z, M_L, q)$ can be calculated as

$$N(z_i, M_{L_j}, q_k) = \int_{z_i}^{z_{i+1}} dz \int_{M_{L_j}}^{M_{L_{j+1}}} \times dM_L \int_{q_k}^{q_{k+1}} dq \int_0^{\infty} dM dY_{\rm SZ} \frac{dV}{dz_{\rm true} d\Omega} \times n(M, z_{\rm true})\, \mathcal{N}(z|z_{\rm true}, \sigma_z)\, \mathcal{N}(M_L|M, \sigma_{M_L}) \times \mathcal{N}(q|Y_{\rm SZ}/\sigma_{Y_{\rm SZ}}, 1) \times \mathcal{N}(\log Y_{\rm SZ}|M, z_{\rm true}, \sigma_{\log_{Y_{\rm SZ}}}), \quad (19)$$

where $n(M_{500c}, z_{\rm true}) \equiv n(M, z_{\rm true})$ is the Tinker et al. (2008) halo mass function (HMF), and $\frac{dV}{dz_{\rm true} d\Omega}$ is the volume element. We parameterize the probability density functions (PDFs) of redshift z, lensing mass M_L, and tSZ S/N q using normal distributions $\mathcal{N}(\mu, \sigma)$ with mean μ and width σ. The scatter in the observable–mass scaling relation $Y_{\rm SZ} - M$ is parameterized using a log-normal $\mathcal{N}(\log Y_{\rm SZ}|M, z_{\rm true}, \sigma_{\log_{Y_{\rm SZ}}})$ with width $\sigma_{\log_{Y_{\rm SZ}}}$. Since the photometric redshift errors for clusters from future surveys are expected to be small compared to the width of the redshift bins described below (LSST Science Collaboration et al. 2009), we neglect redshift errors by setting $z = z_{\rm true}$ with $\sigma_z = 0$; i.e., we assume $\mathcal{N}(z|z_{\rm true}, \sigma_z)$ to be a δ function. Errors in tSZ flux $\sigma_{Y_{\rm SZ}}$ are obtained using the MLE approach described above, and the errors in lensing mass σ_{M_L} are determined using CMB temperature and polarization-based reconstructions.

2.8.1. Monte Carlo Sampling

We solve the above integral using a Monte Carlo (MC) sampling approach to estimate $N(z, M_L, q)$ and its derivatives $\partial N(z, M_L, q)/\partial\theta$ as a function of the parameter under consideration θ. We start by getting the number of haloes $n(M_{500c}, z)$ in the following mass and redshift bins using the Tinker et al. (2008) HMF: $M_{500c} \in [10^{13}, 10^{16}]\, M_\odot$ with $\Delta M_{500c} = 10^{12}\, M_\odot$ and $0.1 \leqslant z \leqslant 3$ with $\Delta z = 0.1$. While statistical uncertainties in the HMF parameters could be potentially important (Artis et al. 2021), we defer their impact on the results to a future work. For each halo, we assign a tSZ flux $Y_{\rm SZ}$ from $\mathcal{N}(\log Y_{\rm SZ}|M, z, \sigma_{\log_{Y_{\rm SZ}}})$ and an associated tSZ S/N q from $\mathcal{N}(q|Y_{\rm SZ}/\sigma_{Y_{\rm SZ}}, 1)$. The tSZ S/N for the halo is obtained by interpolating the S/N look-up table in Section 2.6.1. Lensing mass and redshifts are also assigned using the distributions $\mathcal{N}(M_L|M, \sigma_{M_L})$ and $\mathcal{N}(z|z_{\rm true}, \sigma_z)$. Next we bin the haloes in lensing mass, S/N, and redshift to obtain binned cluster counts $N(z, M_L, q)$ as described below. We repeat the MC sampling approach 100 times to ensure the convergence of cluster counts $N(z, M_L, q)$.

2.8.2. Binning Scheme

We choose 40 and 25 logarithmic bins for lensing mass and tSZ S/N: $M_L \in [10^{12}, 10^{16}]\, M_\odot$ and $q \in [5, 500]$. For redshift, we consider four different binning schemes. In the baseline case, we use $\Delta z = 0.1$ for $0.1 \leqslant z < 1.5$ and conservatively group all high redshift clusters $1.5 \leqslant z \leqslant 3$ in one massive redshift bin similar to that in Madhavacheril et al. (2017). This is due to the difficulties that will be encountered in measuring redshifts of distant clusters. While dedicated follow-up observations are needed to obtain redshifts for clusters at $z \geqslant 1.5$, the absence of an associated signal in multiple LSST bands will still allow us to set a lower limit on the cluster redshifts, and we set this threshold to be $z = 1.5$. Redshifts of clusters with $z < 1.5$ can be obtained using upcoming optical and X-ray surveys (LSST Science Collaboration et al. 2009; Merloni et al. 2012). We also explore other choices for redshift binning: (i) an extremely optimistic case of $\Delta z = 0.1$ for all clusters; (ii) a less conservative choice of $\Delta z = 0.1$ for $0.1 \leqslant z < 2$ and $\Delta z = 1$ for $2 \leqslant z \leqslant 3$; and (iii) a pessimistic setting by ignoring clusters at $z > 1.5$.

2.8.3. Derivatives ∂z, M$_{\rm L}$, q/$\partial\theta$

We estimate derivatives of binned cluster counts $\partial N(z, M_L, q)/\partial\theta$ as a function of parameter θ using a finite difference method. For this, the MC sampling approach must be repeated twice for every parameter perturbing $\theta \rightarrow \theta \pm \epsilon_\theta$. The randomness in sampling, however, can lead to unstable derivatives, and we avoid this by only estimating counts $N(M_L, q, z)$ at the fiducial values of the parameters. For derivatives, we assign weights to haloes based on the ratio of the PDF at the sampled point before and after modifying the parameter values. Subsequently, the weights are decomposed into $w_{\rm Poi}$, $w_{\rm tSZ}$, w_q, w_{M_L}, and w_z with the final weight being the product of all of the individual ones. Here, $w_{\rm Poi} = \frac{[n(M,z)]_{\theta\pm\epsilon}}{[n(M,z)]_\theta}$ quantifies the change in number of haloes when parameter θ is modified. The other weights ($w_{\rm SZ}$, w_q, w_{M_L}, and w_z) are simply the ratio of respective individual PDFs at the sampled point $\frac{[\mathcal{N}(\mu,\sigma)]_{\theta\pm\epsilon}}{[\mathcal{N}(\mu,\sigma)]_\theta}$ described in Section 2.8, and θ is one of the 16 parameters being constrained: observable–mass scaling relation parameters $[\alpha_y, \beta_y, \gamma_y]$ in Equation (9) and $[\sigma_{\log Y}, \alpha_\sigma, \gamma_\sigma]$ in Equation (10); cosmological parameters $[A_s, h, \sum m_\nu, n_s, \Omega_c h^2, \Omega_b h^2, \tau_{\rm re}, w_0]$; and cluster virialization parameters from one of the two models, namely $[\eta_{\rm v}, b_{\rm HSE}]$ in Equation (11) or $[A_{\rm v}, B_{\rm v}]$ in Equation (13).

2.8.4. CMB TT/EE/TE Fisher Matrix

Along with cluster counts, we also make use of the information from primary CMB temperature and polarization power spectra. Since clusters can lens the background CMB, cluster counts will have a nonzero covariance with CMB lensing power spectrum. We make a conservative choice and fully ignore information from CMB lensing power spectrum in this work. We use lensed CMB spectra but do not correct for the lensing-induced correlations. Because of the nonzero covariance between clusters and CMB lensing, we note that this can underestimate the error bars (Green et al. 2017). However, the effect is small, and hence we do not consider it. In a similar vein, we ignore information from the tSZ power spectrum since it must be highly correlated with cluster counts.

We compute CMB Fisher matrices using TT, EE, and TE power spectra ($\ell_{\rm max} = 5000$) obtained using `CAMB` (Lewis et al. 2000) software for the fiducial Planck 2015 cosmology described in Section 2.1. The CMB TT, EE, and TE information comes from the same experiment under consideration. Although we could include Planck information on large scales and in the regions not covered by the experiments in this work, we avoid them in the baseline setup. We also avoid adding S4-Wide information in the regions not covered by S4-Ultra deep. Like in the case of Compton-y maps, we optimally combine information from all frequency channels using the ILC algorithm to compute the residual noise (see Table 1 and Table 2) and foreground spectra (see Section 2.3) in the CMB maps for all three surveys. To generate polarized foregrounds, we assume 2% (3%)

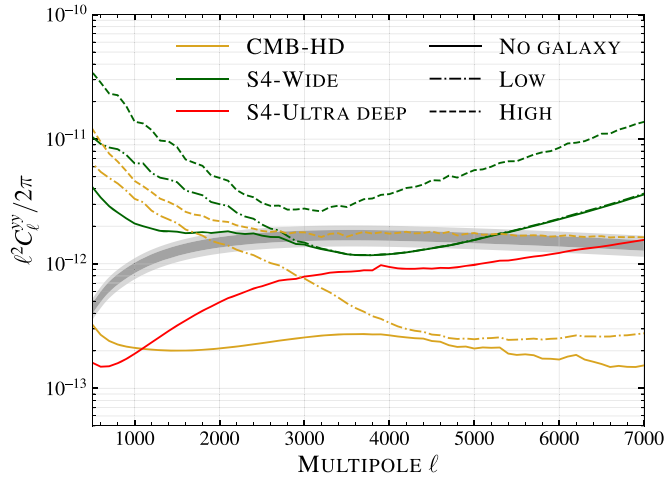

Figure 2. Residual ILC Compton-y noise power spectra N_ℓ^{yy} for the three surveys: CMB-HD in yellow, S4-Wide in green, and S4-Ultra deep in red. Solid curves correspond to noise curves without the inclusion of galactic signals. Dashed–dotted and dashed lines are the residual noise curves in the clean (low) and dirty (high) galactic emission regions. The gray band shows the level of the fiducial tSZ power spectrum along with 1σ, 2σ errors from George et al. (2015). Cluster detection sensitivity for CMB-S4 will be limited by residual CIB signals, while the confusion noise from diffuse tSZ is the dominant source of variance for CMB-HD.

polarization fractions for dusty star-forming (radio) galaxies consistent with measurements from ACT (Datta et al. 2019) and SPT (Gupta et al. 2019). Diffuse kSZ and tSZ signals are assumed to be unpolarized. Information about polarized galactic dust and synchrotron signals comes from pySM3 simulations (see Section 2.3.1).

3. Results and Discussion

3.1. Noise Level in Compton-y Map

Figure 2 shows the residual power in the ILC Compton-y maps (N_ℓ^{yy}) for CMB-HD (yellow), S4-Wide (green), and S4-Ultra deep (red). Solid lines in the figure correspond to noise estimates when galactic emission is not included. CMB-HD and S4-Wide experiments are expected to scan large sky areas ($f_{\rm sky} = 67\%$), and it is unrealistic to ignore galactic emission. Hence for CMB-HD (yellow) and S4-Wide (green) experiments, we also show the noise curves in regions of low (dashed–dotted) and high (dashed) galactic emission as discussed in Section 2.3.1. Since S4-Ultra deep will observe a region with negligible galactic foregrounds (CMB-S4 Collaboration 2019), we only show a solid red line.

In the absence of galactic emission (solid curves), we find the noise level in CMB-HD maps to be much lower than both S4-Wide and S4-Ultra deep surveys. This is primarily due to the reduced level of CIB signals expected in CMB-HD compared to CMB-S4. As described in Section 2.3.2, note that the CIB power at 150 GHz for CMB-HD is lower than CMB-S4 by 17× (Sehgal et al. 2019). The Compton-y maps from CMB-S4 are fully dominated by residual CIB signals on small scales. Residual CIB signals in Compton-y maps can be lowered by nulling CIB signals assuming one or more spectral energy distributions with a constrained ILC (Madhavacheril et al. 2020) or using partial ILC techniques (Bleem et al. 2022). This CIB reduction comes at the cost of higher noise depending on the choice of cleaning. We ignore this here but study the systematics in the recovered cluster tSZ signals due to emissions from DSFGs within clusters (tSZ × CIB) in Section 3.6.

On large scales, we note a change in noise trend and find noise in CMB-HD to be slightly higher than S4-Ultra deep. This is due to a higher atmospheric noise in CMB-HD, as it will be located in Chile (Sehgal et al. 2020) compared to S4-Ultra deep, which will be observing from the South Pole. For S4-Wide, both atmospheric noise and residual CMB signals dominate the large-scale noise, which is much higher than both CMB-HD and S4-Ultra deep surveys. Including information from Planck will improve the noise performance on large scales, but we ignore that as we are primarily interested in $\ell \gtrsim 3000$ for cluster detection.

When galactic emission is included, as expected, the noise increases for both CMB-HD and S4-Wide surveys. For S4-Wide, adding low levels of galactic emission (blue contour in Figure 1) only affects large-scale noise (green dashed–dotted line) as small scales are dominated by residual CIB emission. When looking right through the galactic plane (red contour in Figure 1), residual noise (green dashed) is much higher on all scales. For CMB-HD, any level of galactic emission leads to an increased noise on all scales.

For reference, in the gray band, we show the fiducial tSZ power spectrum along with 1σ, 2σ errors from SPT measurement (George et al. 2015). Comparing the gray band with noise curves, we note that all three surveys can map the peak of the tSZ power spectrum ($3000 \leqslant \ell \leqslant 4500$) with $S/N \geqslant 1$ (CMB-S4 Collaboration 2019).

In addition to the instrumental noise and foregrounds, another source of noise for cluster detection is the confusion noise arising due to the diffuse tSZ signal. Note that the noise curve N_ℓ^{yy} is much lower than tSZ power spectrum for CMB-HD. While this indicates a high S/N measurement of the tSZ power spectrum on all scales, it limits the sensitivity of cluster detection due to the tSZ confusion noise.

3.2. Baseline Results

Our baseline results with no modifications to the cluster tSZ signal are presented in Figures 3–5 and Tables 3 and 4.

3.2.1. Cluster Detection Sensitivity

Figure 3 shows the redshift dependence of the minimum cluster mass required to satisfy the detection threshold criterion $S/N \geqslant 5$. For reference, we also mark the clusters detected at $S/N \geqslant 4.5$ from current surveys: ACT (Hilton et al. 2018, 2021) as blue diamond, Planck (Planck Collaboration et al. 2016b) as red squares, and SPT (Bleem et al. 2015; Huang et al. 2020; Bleem et al. 2020) as black circles. We present two curves for CMB-HD (yellow) and S4-Wide (green): dashed–dotted and dashed curves correspond to sensitivity in regions of low and high levels of galactic emissions, respectively. For S4-Ultra deep, since we do not inject any galactic emission, we only show the solid line containing no galactic foregrounds.

As expected, based on the intuition from Figure 2, minimum detectable cluster mass is lowest for CMB-HD followed by the S4-Ultra deep and S4-Wide surveys. The dominant source of variance for CMB-S4 surveys comes from the residual CIB contamination present in the ILC maps on small scales. We tweaked CMB-S4's configuration to investigate if the residual CIB levels can be lowered further. To this end, we altered the noise level of bands in both CMB-S4 surveys by modifying the

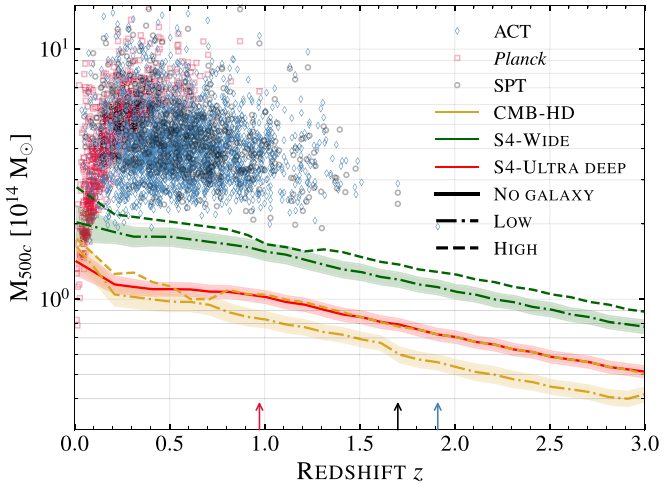

Figure 3. Cluster limiting mass threshold (S/N $\geqslant$ 5) as a function of redshift for future CMB surveys: CMB-HD in yellow, S4-Wide in green, and S4-Ultra deep in red. Different line styles correspond to the estimated sensitivity for different levels of galactic emission: solid for no, dashed–dotted for low, and dashed for high galactic emissions, respectively. See Section 2.3.1 and Figure 2 for more details. Masses and redshifts of clusters with S/N $\geqslant$ 4.5 from currently available tSZ samples are also shown for comparison: ACT (Hilton et al. 2018, 2021) as blue diamonds, Planck (Planck Collaboration et al. 2016b) as red squares, and SPT (Bleem et al. 2015; Huang et al. 2020; Bleem et al. 2020) as black circles. Arrows represent the redshift of the most distant cluster discovered in each survey.

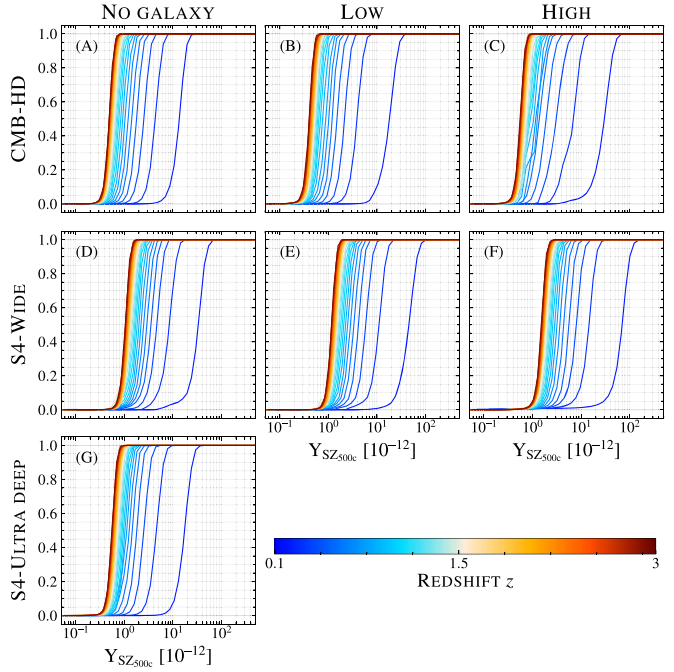

Figure 4. Cluster survey completeness as a function of integrated $Y_{SZ_{500c}}$ signal for the three surveys with different levels of galactic emission. As expected, the curves indicate that surveys with lower instrumental noise and galactic foregrounds will allow us to detect clusters with lower $Y_{SZ_{500c}}$ signals. The redshift trend is due to self-similar evolution of clusters and the residual contamination from CMB and atmospheric noise in the Compton-y maps.

number of detectors in each band. We do not find any improvement, which suggests that the current configuration listed in Table 1 (CMB-S4 Collaboration 2019) is the most optimal for the CMB-S4 cluster survey.

For CMB-HD, since the residual CIB level is expected to be much lower than CMB-S4 in our setup (Sehgal et al. 2019), one could expect the cluster sensitivity to be much higher than CMB-S4. However, the confusion noise from the diffuse tSZ (Holder et al. 2007) sets a noise floor hindering further improvement in sensitivity. Note that the gray signal band in Figure 2 is much higher than the noise curves N_ℓ^{yy} for CMB-HD in yellow. The tSZ confusion noise can be lowered by masking the detected clusters, but we defer a detailed investigation of this to a future work.

The sensitivity in regions of high galactic emission for S4-Wide is worse than the rest of the footprint by roughly 16% at all redshifts. For CMB-HD, the degradation is $\sim$28% for clusters with $z \leqslant 1$ and $\sim$23% overall. While $\lesssim$30% S/N penalty is significant, we note that it is an optimistic estimate given that our model for the galactic emission power spectrum (`S0_d0` dust and `S0_s0` from pySM3 simulations) is a simple power law. It ignores complexities like varying spectral or emissivity indices and non-Gaussianities, which can introduce non-negligible biases to the cluster tSZ signal. As a result, we do not consider the clusters in regions of high galactic emission for subsequent analyses in this work.

While not shown in Figure 3, in the absence of galactic emission, cluster limiting masses reduce by $\sim$7% compared to regions with low levels of galactic emission in the S4-Wide footprint. A significant fraction of this S/N degradation in the presence of galactic emission is for nearby clusters, in agreement with excess large-scale noise, green solid versus green dashed–dotted curves, in Figure 2. For all three surveys, the spike at low redshift in Figure 3 is because we limit S/N calculation to $\theta_{\rm max} = 2'$. While $2' > > \theta_{500c}$ for clusters with $z \gtrsim 0.5$ and hence optimal, our choice of $\theta_{\rm max}$ does not fully encompass the cluster signal for nearby clusters and hence reduces their S/N.

The reason for the decrease in the minimum detectable mass with redshift is twofold. At low redshifts, the cluster S/N degrades because of residual contamination from atmospheric noise and CMB. At high redshifts, according to self-similar evolution of clusters (Kaiser 1986), a cluster with a given mass will have a higher temperature and hence a higher tSZ signal compared to its low redshift counterpart. This leads to an increase in cluster S/N when going from low to high redshifts.

3.2.2. Survey Completeness

Sensitivity can also be expressed in terms of cluster survey completeness as (Planck Collaboration et al. 2016b; Alonso et al. 2016)

$$\chi(Y_{SZ_{500c}}) = \frac{1}{2}\left[1 + \mathrm{erf}\left(\frac{Y^{\rm true}_{SZ_{500c}} - q_{\rm lim}\,\sigma_{Y_{SZ_{500c}}}}{\sqrt{2}\,\sigma_{Y_{SZ_{500c}}}}\right)\right], \qquad (20)$$

where $q_{\rm lim} = 5$ is the detection threshold, $\sigma_{Y_{SZ_{500c}}}$ is the measurement uncertainty of the integrated $Y_{SZ_{500c}}$ signal estimated in Section 2.6.1, and $Y^{\rm true}_{SZ_{500c}}$ is the true $Y_{SZ_{500c}}$ flux. Cluster limiting mass as a function of redshift shown in Figure 3 represents 50% survey completeness. In Figure 4, we show the completeness as a function of $Y_{SZ_{500c}}$ for all three surveys for different levels of galactic emission. Here, $Y_{SZ_{500c}}$ is the integrated Compton signal within the virial radius R_{500}. Colors represent cluster redshift with $z = 0$ in blue and $z = 3$ in red. Higher experimental sensitivity will result in steeper curves. It will also push the curves to the left enabling detection

Table 3
Forecasted Number of Clusters from Future SZ Surveys with S/N $\geqslant 5$ in Regions with Different Levels of Galactic Emission

Experiment	Baseline Footprint			Dirty Footprint			Full Footprint		
	$f_{\rm sky}$	Total	$z \geqslant 2$	$f_{\rm sky}$	Total	$z \geqslant 2$	$f_{\rm sky}$	Total	$z \geqslant 2$
CMB-HD	50%	325,860	11095	17%	76,165	1894	67%	402,025	12,989
S4-Wide		75,701	992		17,541	166		93,242	1158
S4-Ultra deep	3%	13699	341		…		3%	13699	341

of clusters with a lower $Y_{\rm SZ_{500c}}$ signal. This is evident from the figure, where we note that curves move from lower to higher values of $Y_{\rm SZ_{500c}}$ for increasing levels of galactic emission (left to right). The slopes of individual lines also decrease in the same order. We note the same pattern when going from low-noise to high-noise surveys (CMB-HD → S4-Ultra deep → S4-Wide) and also from low to high cluster redshifts (blue to red). The redshift trend is because of: (a) S/N degradation for low redshift clusters due to residual contamination from atmospheric noise and CMB and (b) S/N improvement due to self-similar evolution for higher redshift clusters. The significant S/N penalty for lowest redshifts $z \lesssim 0.3$ is due to the hard cutoff $\theta_{\rm max} = 2'$ used for S/N calculation. See Section 3.2.1 for more discussion.

Based on these results, we find that S4-Wide shall detect (at 5σ) all galaxy clusters with an integrated Compton $Y_{\rm SZ_{500c}} \geqslant 10^{-12}$ at $z \geqslant 1.5$ over the large area survey footprint ($f_{\rm sky} = 50\%$) as shown in panel (E) of Figure 4. Furthermore, S4-Ultra deep shall detect (at 5σ) all galaxy clusters with an integrated Compton $Y_{\rm SZ_{500c}} \geqslant 5 \times 10^{-13}$ at $z \geqslant 1.5$ over the de-lensing survey footprint ($f_{\rm sky} = 3\%$) shown in the bottom panel (G). The sensitivity of CMB-HD is roughly similar to S4-Ultra deep but over a large region $f_{\rm sky} = 50\%$ of sky as shown in panel (B).

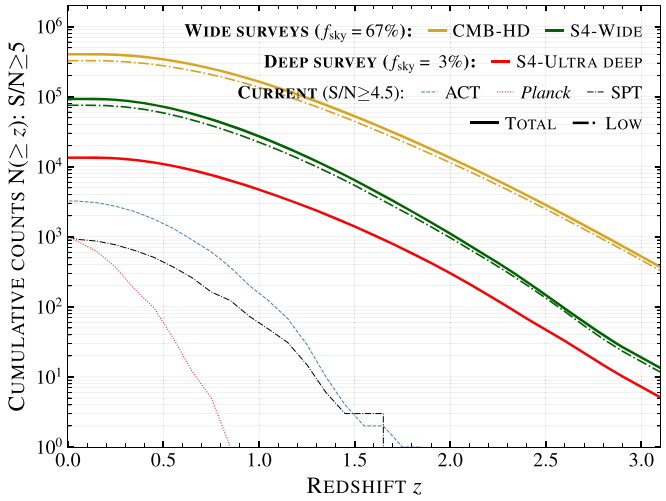

Figure 5. Cumulative cluster redshift distribution for future (current) SZ samples are shown as thick (thin) curves. For CMB-HD (yellow) and S4-Wide (green), we show two curves: dashed–dotted corresponds to clusters expected in the baseline (low galactic emission) footprint ($f_{\rm sky} = 50\%$) and solid corresponds to the total clusters expected in the combined low and high galactic emission regions. CMB-S4 is expected to detect close to 1000 (350) clusters at $z \geqslant 2$ in the baseline footprint $f_{\rm sky} = 50\%(3\%)$ with the S4-Wide (S4-Ultra deep) survey. The number of $z \geqslant 2$ is more than an order of magnitude larger for CMB-HD compared to CMB-S4. The enormous improvement in the sensitivity of high redshift clusters for future surveys compared to current experiments (thin lines) is evident from the curves.

3.2.3. Cluster Counts

We present a cumulative redshift distribution of clusters expected from the three surveys in Figure 5: CMB-HD in yellow, S4-Wide in green, and S4-Ultra deep in red. Cluster counts are obtained by sampling Tinker et al. (2008) HMF using the MC sampling approach discussed in Section 2.8.1. Dashed–dotted lines for CMB-HD and S4-Wide correspond to clusters expected from regions with low galactic foregrounds. Solid curves are the total number of clusters from the full footprint, i.e., a combination of both low and high galactic emission regions, and the split between the two regions can be found in Table 3. Like in the previous Sections, galactic foregrounds are absent for S4-Ultra deep. For comparison, we show the currently available SZ cluster samples (S/N $\geqslant 4.5$) from ACT (Hilton et al. 2018, 2021) as blue dashed, Planck (Planck Collaboration et al. 2016b) as red dotted, and SPT (Bleem et al. 2015, 2020; Huang et al. 2020) as black dashed–dotted curves.

S4-Wide shall detect close to 75,000 clusters in the baseline footprint ($f_{\rm sky} = 50\%$) while the S4-Ultra deep will obtain ∼14,000 clusters in CMB-S4's de-lensing footprint ($f_{\rm sky} = 3\%$). While most of the low redshift $z \lesssim 1$ clusters will be part of the LSST or eROSITA cluster samples (LSST Science Collaboration et al. 2009; Merloni et al. 2012), the redshift independent property of the tSZ signal will open the unique high redshift discovery space for future CMB surveys. For example, S4-Wide (S4-Ultra deep) is expected to detect 1000 (350) clusters at $z \geqslant 2$. The number of clusters expected from CMB-HD is three times greater than that from S4-Wide. In the high redshift regime $z \geqslant 2$, the expected number for CMB-HD is more than an order of magnitude higher than CMB-S4. In Table 4, we give the median masses and redshifts of clusters in the baseline footprint from all three surveys. Average lensing mass estimates of the cluster sample using both temperature and polarization CMB-cluster lensing is also given in the table. While CMB temperature returns a higher lensing S/N for S4-Wide, we find a polarization channel to dominate the S/N for S4-Ultra deep. This is due to the higher noise floor set by foreground signals along with additional strategies used to mitigate foreground-induced bias in temperature-based lensing reconstruction. The same is true for CMB-HD but to a much lower extent since the variance from CIB is highly suppressed for CMB-HD (Sehgal et al. 2019). We report median mass and lensing estimates for both the full sample and also for clusters with $z \geqslant 2$.

Table 4
Median Mass and Redshift of Cluster Sample from the Future SZ Surveys in Their Baseline Footprint along with the CMB-cluster Lensing Mass Constraints

Experiment	$z^{\rm med}$			$M_{\rm 500c}^{\rm med}$ [10^{14} $M_\odot$]	
$\Delta M_{\rm lens}^{\rm stack}$ [$10^{14} M_\odot$]					
		All	$z \geqslant 2$	All	$z \geqslant 2$
CMB-HD	0.7	0.8	0.4	0.002	0.02
S4-Wide	0.8	1.6	0.8	0.02	0.31
S4-Ultra deep	0.7	1.0	0.6	0.05	0.55

3.3. Change in Sensitivity due to Changes in Virialization

Modifying cluster virialization alters the cluster tSZ signal from clusters, which in turn affects the tSZ S/N. This is illustrated using the change in the minimum detectable cluster mass as a function of redshift in Figure 6 for S4-Wide with low levels of galactic emission. The thick solid black line is the baseline curve, the same as the green dashed–dotted curve in Figure 3. The thin dashed curves are for model 1 when we vary the virialization efficiency from $\eta_{\rm v} \in [0.9,\ 1.1]$ based on Equations (11) and (12). As expected, the minimum detectable masses decrease for $\eta_{\rm v} > \eta_{\rm v}^{\rm fid} (=1.0)$. The number of high redshift $z \geqslant 2$ clusters from S4-Wide drop (increase) by two times for $\eta_{\rm v} = 0.9(1.1)$ compared to 992 clusters for the fiducial value $\eta_{\rm v}^{\rm fid} = 1.0$ (see Table 3).

The thick pink dashed–dotted curve is for model 2 based on Equation (13). It is similar to our baseline case (black), and we get roughly a 10% overall increase in the number of clusters consistent with the trend in Figure 6.

3.4. Fisher Forecasts

Now we turn to parameter constraints using the Fisher formalism presented in Section 2.8. We combine $N(z, M_L, q)$ with primary CMB information from the three surveys to forecast standard errors on the parameters governing one of the two virialization models along with the $Y_{\rm SZ} - M$ scaling relation (Equation (9)) and cosmological parameters. For cosmology, we focus on two-parameter extension to Lambda cold dark matter (ΛCDM) to include the sum of neutrino masses $\sum m_\nu$ and dark energy equation of state w_0. Unless otherwise stated, *cluster counts* $N(z, M_L, q)$ in the rest of this section includes temperature- and polarization-based CMB-cluster lensing mass calibration. The baseline redshift binning adopted was $\Delta z = 0.1$ for $0.1 \leqslant z < 1.5$ and one massive redshift bin for all high redshift clusters $1.5 \leqslant z \leqslant 3$. A Planck-like prior has been assumed for optical depth to reionization $\sigma(\tau_{\rm re}) = 0.007$.

We also look into the following: (a) individual constraints from primary CMB and cluster counts, (b) importance of CMB-cluster lensing-based mass calibration, (c) impact of high redshift clusters and redshift binning, and (d) the effect of $\tau_{\rm re}$ prior. These checks are limited to S4-Wide only.

3.4.1. Cosmology and Cluster Virialization Model

In Figure 7, we present the marginalized constraints (68% CL) on $\theta \in [\eta_{\rm v}, b_{\rm HSE}, A_{\rm v}, B_{\rm v}, \sum m_\nu, w_0]$ from all three surveys: CMB-HD in yellow, S4-Wide in green, and S4-Ultra deep in red. The lower and upper diagonals correspond to constraints for cluster virialization models 1 and 2, respectively.

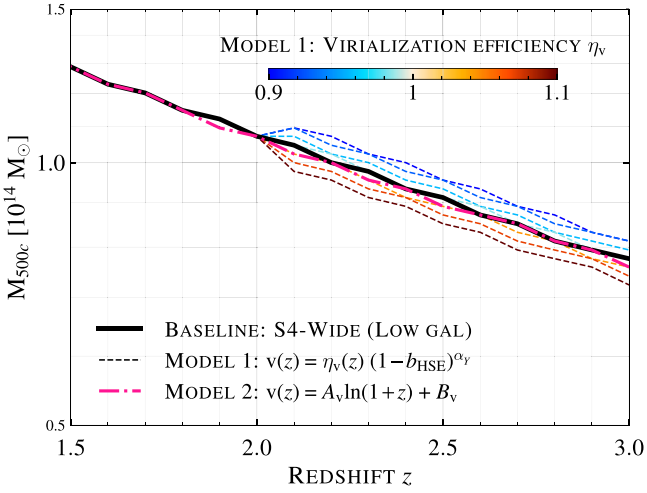

Figure 6. Dependence of cluster detection sensitivity on the virialization model. The black curve is the baseline case for S4-Wide survey in the region with low galactic emission, the same as the green dashed–dotted curve in Figure 3. The thin dashed curves are for model 1 with virialization efficiency parameter ranging from $\eta_{\rm v} \in [0.9$ (blue), 1.1 (red)]. The thick pink dashed–dotted curve is for model 2 with $A_{\rm v} = 0.155$ and $B_{\rm v} = 0.189$.

The CMB-S4 and CMB-HD experiments can provide stringent constraints on the dark energy equation of state $\sigma(w_0)$ and the sum of neutrino masses. We obtain 1%–2% on $\sigma(w_0)$ from CMB-S4: 1.2% (1.8%) from S4-Wide (S4-Ultra deep) and 1% jointly from both CMB-S4 surveys. CMB-HD will provide sub-percent (0.5%) level constraints on w_0. For neutrino masses, we obtain $\sigma(\sum m_\nu) = 28$ meV(45 meV) from S4-Wide (S4-Ultra deep), 23 meV jointly from both, and 13 meV from CMB-HD, enabling a $\sim 2.5\sigma$–4.5σ detection of the sum of neutrino masses from both CMB-S4 and CMB-HD assuming a normal hierarchy lower limit of 60 meV. Although not shown in the figures, both experiments provide $\lesssim$1% constraints on the scalar fluctuation amplitude A_s, Hubble parameter $\sigma(h)$, and dark matter density $\sigma(\Omega_c h^2)$. Adding large-scale information from Planck has a negligible impact on the constraints from S4-Wide and CMB-HD, while it improves the cosmological constraints from S4-Ultra deep by 5%–10%.

Results for the first virialization model in Equation (11) are shown in the lower diagonal of Figure 7. We find that CMB-S4 clusters can help constrain $\sigma(\eta_{\rm v})$ at the 2%–4% level, while CMB-HD can provide sub-percent level constraints. However, note that this assumes we have 100% knowledge about the astrophysics of low redshift clusters, which is not fully true but has been rapidly advancing (see recent review by Mroczkowski et al. 2019). Both experiments can provide sub-percent constraints on the HSE bias $1 - b_{\rm HSE}$. While $\eta_{\rm v}$ only modifies the tSZ signal of clusters at $z \geqslant 2$ and is only constrained by them, low redshift clusters are also important in breaking the degeneracies between other cosmological/scaling relation parameters and $\eta_{\rm v}$. For example, if we only consider clusters at $z \geqslant 2$, $\eta_{\rm v}$ is highly degenerate with parameters like $b_{\rm HSE}$ or σ_8, and adding low redshift information almost entirely breaks the degeneracies with other parameters.

The upper diagonal of Figure 7 shows the results for the second cluster virialization model in Equation (13). In this case, we obtain $\sigma(A_{\rm v}) = 0.05$ (0.1) from S4-Wide (S4-Ultra deep) for the redshift evolution parameter of the virialization, corresponding to $\sim$33% jointly from the two CMB-S4 surveys. For $\sigma(B_{\rm v})$, we get 5% and 8% from the two CMB-S4 surveys and

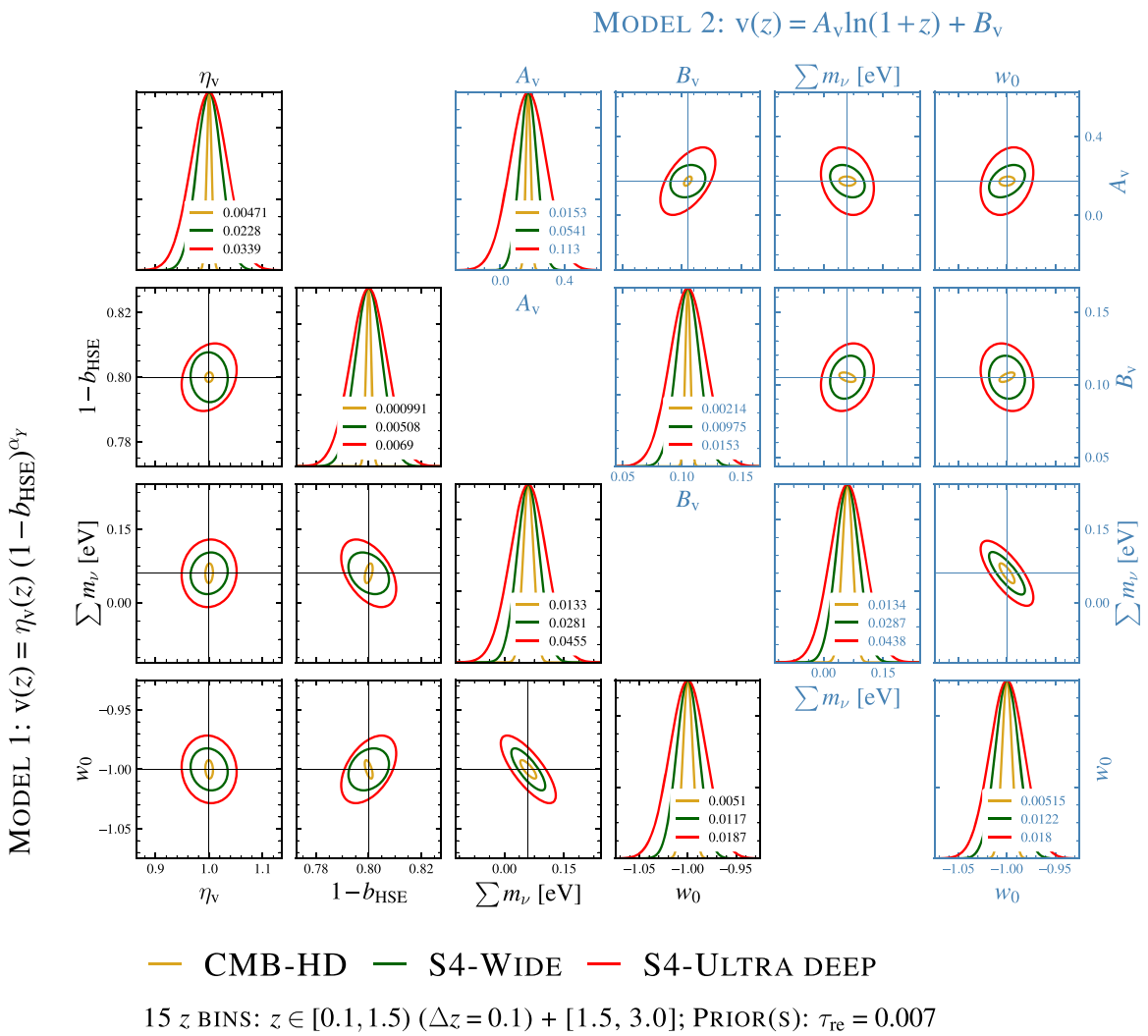

Figure 7. Marginalized Fisher constraints (68% CL) obtained by combining information from primary CMB spectra (TT/EE/TE) and cluster counts $N(z, M_L, q)$: CMB-HD is in yellow, S4-Wide in green, and S4-Ultra deep in red. We use a Planck-like prior $\sigma(\tau_{\rm re}) = 0.007$ for all surveys. Both surveys can reduce the uncertainty on the dark energy equation-of-state parameter $\sigma(w_0)$ to $\lesssim$1%. Combining primary CMB with clusters will also enable $\sim$2.5σ–4.5σ detection of the neutrino masses. The lower and upper diagonals represent cluster virialization models 1 and 2, respectively. *Model 1:* Cluster virialization efficiency $\eta_{\rm v}$ can be constrained to an accuracy of 2%–4% by S4-Wide and S4-Ultra deep, while CMB-HD can provide sub-percent level constraints. All surveys provide <1% constraints on the HSE bias parameter. *Model 2:* CMB-S4 can provide 33% and $\sim$4% constraints on $A_{\rm v}$ and $B_{\rm v}$ parameters, while CMB-HD reduces the uncertainties on both parameters by $\geqslant$ three times. Errors on other parameters do not change significantly between the two cluster virialization models.

$\sim$4% jointly. CMB-HD will reduce the measurement uncertainty on these two parameters by more than three times.

Modifying cluster virialization from model 1 to model 2 does not introduce statistically significant differences in other parameter constraints as can be seen by comparing the lower and upper diagonals in Figure 7.

3.4.2. Observable–Mass Scaling Relation

The scatter in the $Y_{\rm SZ} - M$ scaling relation is constrained to the 13%–16% level by CMB-S4, and to the 2% level by CMB-HD. The 1σ errors on mass and redshift evolution parameters of the relation are $\sigma(\alpha_\gamma) = 0.01$, $\sigma(\beta_\gamma) = 0.02$, and $\sigma(\gamma_\gamma) = 0.02$ for S4-Wide. When switching from model 1 to model 2, we note a strong degeneracy between $A_{\rm v}$ and γ_γ since they both probe the redshift evolution of the tSZ signal. The mass and redshift evolution parameters of the log-normal scatter (α_σ and γ_σ) are an order of magnitude worse. The numbers are similar or sometimes slightly better for S4-Ultra deep, which is because of a better lensing S/N per cluster for S4-Ultra deep. We note that CMB-HD can improve constraints on the $Y_{\rm SZ} - M$ scaling relation parameters by roughly an order of magnitude compared to CMB-S4.

3.4.3. CMB versus Cluster Counts

In Figure 8, we present the constraints (68% CL) separately from CMB TT/EE/TE (orange dotted) and cluster counts (purple dashed) for S4-Wide. The green solid curves correspond to the joint CMB and cluster count constraints. As before, lower and upper diagonals correspond to virialization models 1 and 2. CMB spectra are insensitive to cluster virialization parameters ($\eta_{\rm v}$, $b_{\rm HSE}$, $A_{\rm v}$, $B_{\rm v}$), and hence, the orange dotted curves are not shown for those parameters. However, CMB still helps in constraining them by breaking degeneracies with other parameters. That is the reason for the difference between the purple dashed (cluster counts) and green solid (joint constraints) curves. For other parameters, CMB spectra add minimal to modest levels of information compared to clusters. However, since CMB and cluster counts prefer

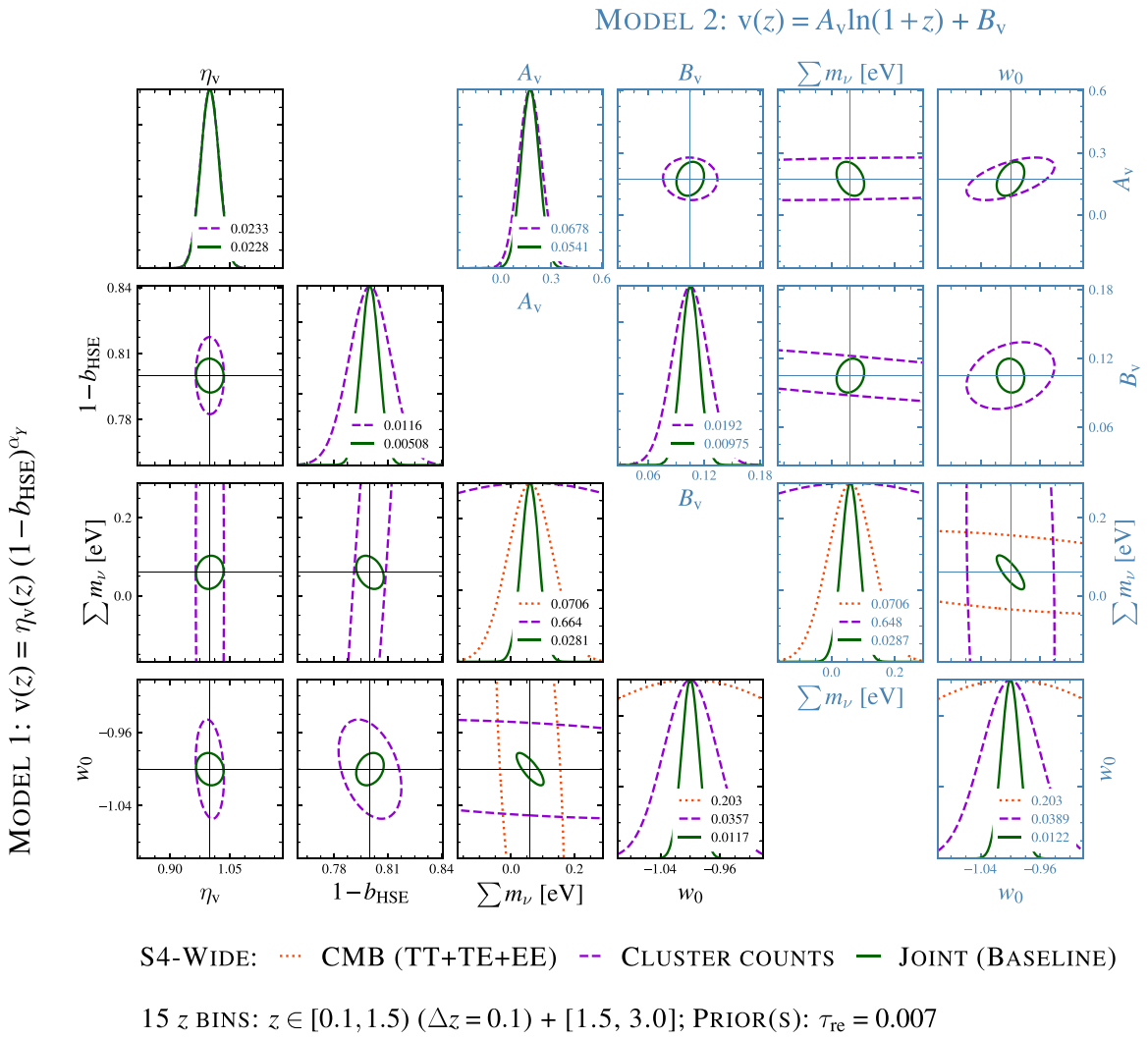

Figure 8. Individual constraints (68% CL) from CMB TT/EE/TE spectra (orange dotted) and cluster counts (purple dashed) are shown. The combination of the two, our baseline setup, is shown as the green solid curves. The nearly orthogonal degeneracy directions of CMB spectra and cluster counts on structure growth parameters provide excellent joint constraints compared to either of them individually on $\sigma(\sum m_\nu)$ and $\sigma(w_0)$. Only S4-Wide is shown.

different nearly orthogonal degeneracy directions, the joint constraints offer remarkable improvements compared to either of them individually. For example, constraints on the sum of neutrino masses improve by $\times 2.5$, from $\sigma(\sum m_\nu) = 70$ meV to 28 meV, when adding cluster counts to primary CMB spectra.

3.4.4. Importance of Lensing Masses

CMB-cluster lensing-based mass calibration is critical to obtain the results described above. To highlight the importance, we present constraints with (green solid) and without (pink dashed) CMB-cluster lensing information in Figure 9. When CMB-cluster lensing in excluded, we simply bin clusters in tSZ S/N q and redshift z: $N(z, q)$. Since both cosmological and $Y_{SZ} - M$ scaling relation parameters affect the cluster redshift and tSZ S/N distributions, they can be constrained even in the absence of lensing masses albeit rather weakly (Louis & Alonso 2017). For example, errors on cosmological parameters $\sigma(\sum m_\nu) = 60$ meV and $\sigma(w_0) = 0.03$ both degrade by more than two times for pink without lensing compared to green curves with lensing mass calibration. Errors on virialization model parameters also degrade similarly by three times or more without lensing mass information.

3.4.5. Impact of High Redshift Clusters and Redshift Binning

The constraints presented above have been derived by binning clusters at $z \geqslant 1.5$ in one massive high redshift bin. This is a conservative approach to take into account the difficulty of obtaining redshifts for distant clusters. We modify this choice using: case (i) an optimal setting with $\Delta z = 0.1$ for all clusters; case (ii) a less conservative setting with $\Delta z = 0.1$ for $0.1 \leqslant z < 2$ and $\Delta z = 1$ for $2 \leqslant z \leqslant 3$; and case (iii) a pessimistic setting by ignoring clusters at $z > 1.5$.

Case (i): We note a $\times 3.8$ better constraint on $\sigma(\eta_v) = 0.0076$ compared to the baseline case $\sigma(\eta_v) = 0.0228$ (see green curve in Figure 7). Constraints on other virialization model parameters b_{HSE}, A_v, B_v also improve by 20%–30%. Similar improvements are seen for h, w_0 but this optimistic redshift binning scheme has a negligible (<10%) impact on A_s, $\sum m_\nu$, and $\Omega_c h^2$.

Case (ii): In this case, we see a threefold improvement on $\sigma(\eta_v) = 0.0092$ and a 15% improvement on b_{HSE}, A_v, B_v compared to the baseline case, but this setting has a negligible (<10%) impact on other parameters.

Case (iii): Since η_v only affects clusters with $z \geqslant 2$, we do not constrain η_v with this pessimistic setting even though this is one

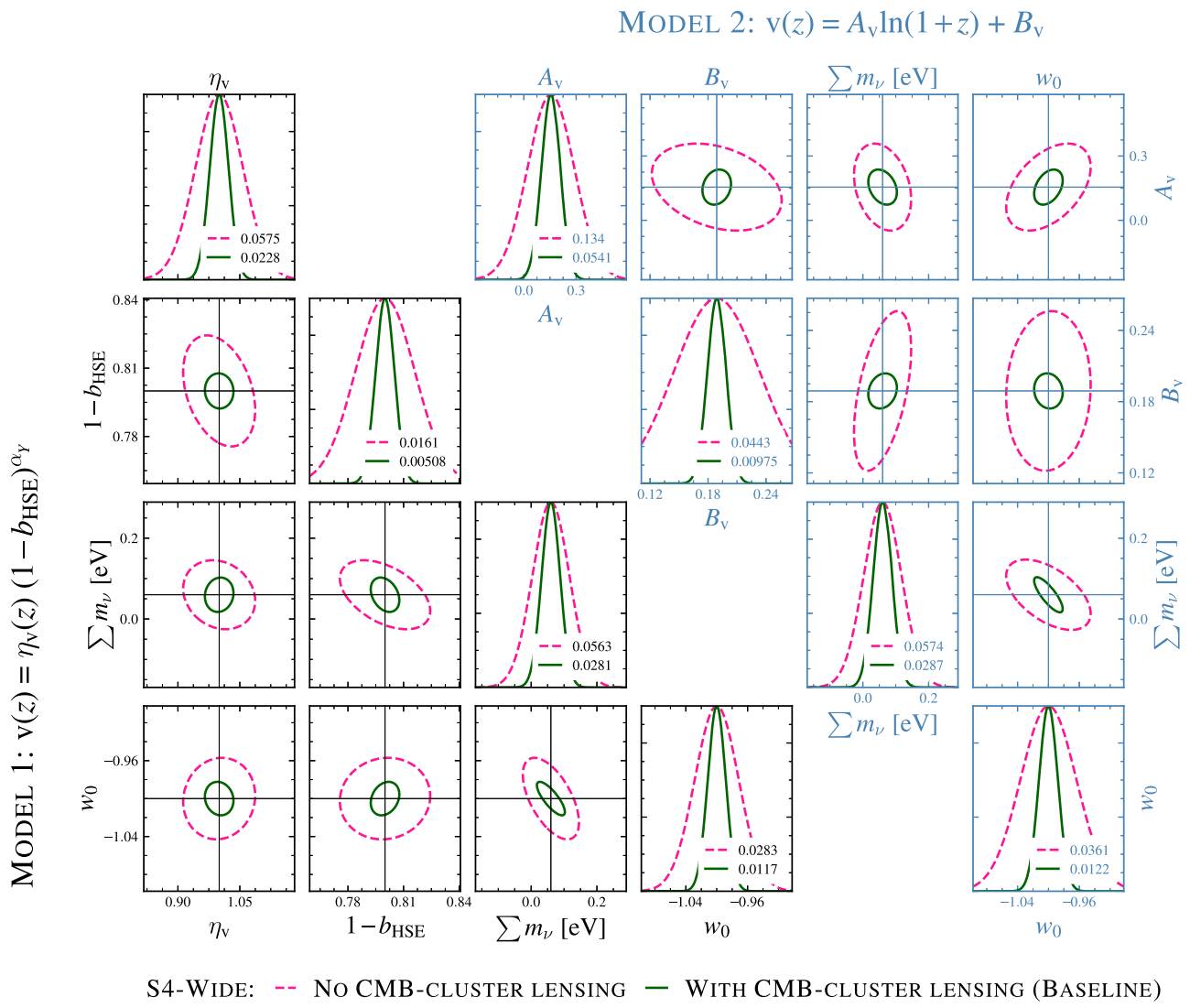

Figure 9. Importance of CMB-cluster lensing mass calibration for cluster counts. The green curves are the same in the left panels, while the pink dashed curves are constraints obtained without CMB-cluster lensing information. Ignoring lensing mass calibration degrades the constraints significantly for all parameters. Ellipses are 68% CL regions, and only S4-Wide is shown.

of the main goals of this work. Nevertheless we perform this test to address the challenges in obtaining redshifts and understanding the survey selection for clusters at $z > 1.5$. We note up to 15% degradation in constraints on cosmological parameters indicating that clusters with $z \leqslant 1.5$ dominate cosmological constraints. The other virialization model parameter constraints, $b_{\rm HSE}$ and B_ν worsen by 15%, while A_ν, controlling the redshift evolution of model 2, degrades by more than 60%.

3.4.6. Effect of $\sigma(\tau_{\rm re})$ Prior

Here we check the effect of the Planck-like prior adopted in the forecasts above. Since a higher optical depth would suppress small-scale CMB anisotropies, $\tau_{\rm re}$ has significant correlation with parameters like h, $\Omega_c h^2$, $\sum m_\nu$, and w_0 and the choice of $\sigma(\tau_{\rm re})$ prior can affect other parameter constraints. Subsequently we check the effect of replacing Planck $\sigma(\tau_{\rm re}) = 0.007$ with (i) no $\sigma(\tau_{\rm re})$ prior and (ii) a cosmic variance limited measurement $\sigma(\tau_{\rm re}) = 0.002$, for example as expected from the LiteBIRD or CORE satellites (Hazra et al. 2018; Di Valentino et al. 2018). Even though this has an effect on CMB-only constraints on all of the parameters listed above, we note significant effects only on $\sum m_\nu$ and $\Omega_c h^2$ with the joint CMB and cluster count information.

Removing $\tau_{\rm re}$ prior degrades $\sigma(\sum m_\nu)$ by $\times 1.5$. With $\sigma(\tau_{\rm re}) = 0.002$, $\sigma(\sum m_\nu)$ improves by $\times 1.3$–1.5 from the three surveys. We obtain a similar level of changes on $\sigma(\Omega_c h^2)$ with the two settings. The prior on $\tau_{\rm re}$ does not affect virialization model parameter constraints.

3.5. Dependence on Total Survey Time

Thus far, the forecasted cluster number counts and the cosmological constraints are obtained using noise levels in Table 1 expected to be achieved at the end of survey periods. Given that S4-Wide is expected to start operations close to the end of this decade, these constraints may not be achieved until

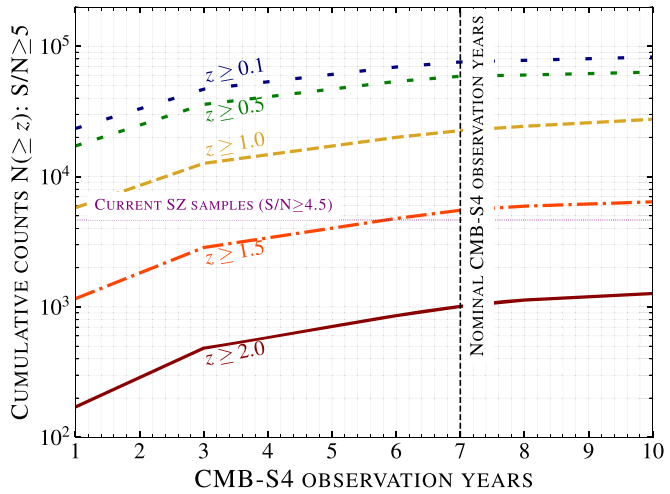

Figure 10. Cumulative cluster counts for S4-Wide shown as a function of number of observation years. The number of clusters in a 1 yr S4-Wide sample will surpass the currently available SZ cluster samples (purple dashed–dotted line). The counts cannot be simply scaled from the baseline observing period of 7 yr because of residual foreground signals that dominate small scales and hence have a major impact on high-z clusters. For example, the actual $z \geqslant 2$ clusters at the end of the first year are two times lower than what will be obtained using a simple noise scaling.

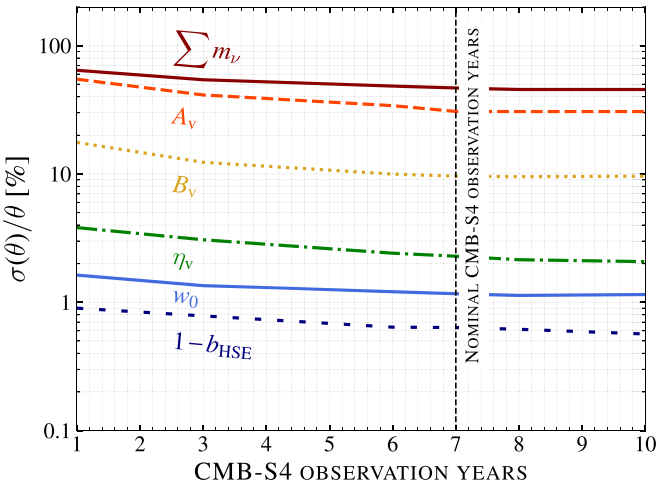

Figure 11. Relative cosmological constraints that can be obtained by combining clusters with primary CMB as a function of S4-Wide observing years. Our results indicate that S4-Wide can return remarkable cosmological constraints compared to current limits even in its first few years of observation. S4-Wide, at the end of the first few years of observations, can also place compelling constraints on the virialization mechanism of high redshift clusters that is currently unconstrained.

the middle of next decade. In this section, we check the dependence of cluster counts and cosmological constraints as a function of observing time for S4-Wide. For this test we simply scale the noise levels in each band by $\sqrt{N_{\rm years}/N_{\rm baseline}}$ where $N_{\rm baseline} = 7$ yr. We go from 1 yr to 10 yr. Note that this simple scaling assumes full deployment at the start of the survey, which could be unrealistic, and the noise scaling may be slightly more complicated for the first few years in reality.

In Figure 10, we show the cumulative cluster counts for clusters above multiple redshifts as a function of the number of S4-Wide observation years. It is evident from the figure that the S4-Wide cluster sample, with ∼20,000 clusters, will surpass the current SZ samples from ACT, Planck, and SPT (purple dotted line) even at the end of the first year of observation. In fact, at the end of the first year, the S4-Wide sample will have close to 5000 clusters at $z \geqslant 1$, similar to the total number of current SZ clusters at all redshifts. It is also worth noting that we use an S/N threshold of 5 for S4-Wide, while the current SZ samples shown here use 4.5.

The number of clusters expected at the end of each year cannot be obtained from baseline results (7 yr) using a simple noise scaling because of residual foregrounds in the Compton-y maps. Since the residual foregrounds (mostly CIB) dominate small scales, the impact of residual foregrounds is more important for high redshift clusters that span a smaller angular extent on the sky. For example, scaling S4-Wide clusters at $z \geqslant 2$ from Table 3 should return $N^{1\ \rm year}_{\rm clus}(z \geqslant 2) = \sqrt{7}\,(992) = 375$ clusters while we have $\lesssim$200 clusters (two times lower) at the end of year 1 in Figure 10.

Cosmological constraints from clusters and primary CMB as a function of S4-Wide observation years are presented in Figure 11. Similar to cluster forecasts, noise levels in each band are scaled from Table 1 for each year to obtain the CMB Fisher matrix. The improvement in constraints is not dramatic as a function of observing years, and this is primarily because of different degeneracy directions in the parameter space probed by clusters and primary CMB. However, note that cluster cosmology is not the only science driver for CMB-S4. It has a broad range of science goals including the measurement of light relic density and the production legacy catalogs in millimeter/submillimeter wavelengths that require the proposed $N_{\rm baseline} = 7$ yr (CMB-S4 Collaboration 2019) to produce wide and deep CMB maps. With ∼200 (400) clusters at $z \geqslant 2$ at the end of year 1 (3), we find that S4-Wide can make a giant leap toward understanding the astrophysics and the onset of the virialization mechanism of high redshift clusters, which are completely unconstrained currently.

3.6. Effect of Cluster Correlated Foreground Signals

In our baseline approach, we ignored cluster correlated foreground signals, namely the cluster kSZ signal and emission from DSFGs and RGs within clusters. For clusters close to detection limits for all three surveys considered here, cluster kSZ signals are less important as they are expected to be much smaller than the tSZ signal. Moreover, kSZ can be both positive or negative depending on the direction of the radial motion and hence only acts as an additional source of variance in our analysis. On the other hand, emission from DSFG and radio galaxies, since they are always positive, can fill in the tSZ decrements thereby potentially contaminating tSZ measurements. While the presence of DSFG signals within clusters has been identified in Planck clusters (Planck Collaboration et al. 2016d), Melin et al. (2018a) reported that signals from DSFGs degrade the completeness of the Planck cluster catalog by $\lesssim$10% and showed that this contamination has a negligible impact on cosmological parameter inference. However, the Planck cluster sample deals with massive low redshift clusters where the star formation has been observed to be highly suppressed (Popesso et al. 2015). Furthermore, the cluster tSZ signal goes as $M^{5/3}$ while DSFG signals are roughly linear. As a result, DSFG contamination may be insignificant for Planck clusters. In this work, we are particularly interested in low-mass ($M_{500c} \lesssim 10^{14} M_\odot$) and high redshift $z \geqslant 1.5$ clusters, near the peak of cosmic star formation history, to constrain cluster

astrophysics; hence, dust contamination might potentially be important.

We check the impact of cluster correlated signals using Websky (Stein et al. 2020) and MDPL2 (Y. Omori 2022, in preparation) simulations. Websky[14] simulations are publicly available, while MDPL2[15] is currently under preparation and obtained using private communication. For this test, it is important that the correlation between tSZ and CIB signals in Websky and MDPL2 simulations is in agreement with the measurements reported in the literature. Defining the correlation coefficient between the two as $\rho_{\rm tSZ\ \times\ CIB} = \frac{C_\ell^{\rm tSZ\ \times\ CIB}}{\sqrt{C_\ell^{\rm tSZ\ \times\ tSZ} C_\ell^{\rm CIB\times CIB}}}$, the value for Websky (MDPL2) at $\ell = 3000$ is $\sim$0.25 (0.17). These are in reasonable agreement with the values reported by SPT 0.2 ± 0.12 (George et al. 2015) and Planck 0.18 ± 0.07 (Planck Collaboration et al. 2016e). To this end, we extract $2^\circ \times 2^\circ$ cutouts of kSZ and DSFG emissions around haloes in the mass and redshift grid used for S/N calculations: $\log M_{500c} \in [13, 15.4]\ M_\odot$ with $\log \Delta M = 0.1\ M_\odot$ and $z \in [0.1, 3]$ with $\Delta z = 0.1$. Before extraction, we mask sources with flux at 150 GHz above $S_{150} \sim 6$ mJy. We also apply a frequency-dependent scaling factor for Websky DSFG signals to match SPT measurements. At 150 GHz, this map scaling factor is 0.75 to match Websky to SPT $D_{\ell_{3000}}^{150} = 12 \mu K^2$ (Reichardt et al. 2021). No such scaling was applied to MDPL2 simulations. In both cases, we pick 100 cutouts for every point in the M_{500c}, z grid. Due to the availability of a single Websky/MDPL2 mock sky realization, the number of kSZ/CIB signals available for this test reduces significantly for clusters with mass $M_{500c} \gtrsim 3 \times 10^{14} M_\odot$ at $z \gtrsim 2$. Hence, we limit this test to clusters below this mass and redshift range. We inject the cluster correlated signals from Websky/MDPL2 into our simulations in all of the frequency bands along with cluster tSZ signal, experimental noise, CMB and other astrophysical foregrounds described in Section 2.1, which are then passed through the ILC pipeline.

For high redshift ($z \geqslant 1$) clusters near the detection limit, we note that DSFGs within clusters shift the tSZ-based cluster masses slightly lower. However, the bias is subdominant compared to statistical uncertainties at roughly the $\leqslant 0.2\sigma$ level for all three surveys. The bias is almost zero for low redshift clusters. As expected, cluster kSZ signals have a negligible impact on the recovered tSZ signals.

Both Websky and MDPL2 do not contain emission from RGs within clusters. Subsequently, we choose an extremely conservative test to assess the impact of RGs within clusters on the recovered tSZ signals. We inject a constant flux of $S_{150} = 0.1$ mJy or 0.5 mJy for all clusters where the latter roughly matches the point source sensitivity (3σ) at 90 GHz for the CMB-S4 survey (CMB-S4 Collaboration 2019). The signal is scaled to other bands assuming a spectral index $\alpha_{\rm radio} = -0.6$ (Everett et al. 2020). This test is limited to S4-Wide only. We find that an $S_{150} =$ 0.1 mJy (0.5 mJy) can bias tSZ measurements low by 0.1–0.2σ ($\gtrsim 1\sigma$). While a 1σ systematic error is large, we note that our model for RGs is unrealistic, and hence our results should only be interpreted as an upper limit of the systematic error.

Our simple RG model can be potentially replaced using the Websky simulations, which are currently being upgraded to include RG signals correlated with the underlying dark matter. Similarly the limitation due to the smaller number of Websky or MDPL2 haloes at the high-mass end can be addressed using multiple realizations of the millimeter-wave sky, as released recently by Han et al. (2021) using deep learning techniques, for example. We leave these detailed studies for a future work.

3.6.1. Impact on Sample Purity due to Point Sources

Given that point sources in the maps can be misclassified as clusters, we check the effect of point sources using 100 noise-only simulations. The simulations for this test include astrophysical foregrounds, CMB, experimental noise and point source signals. Cluster tSZ signal is ignored here. We model the point source signals in three different ways.

In the first case, we add the cluster correlated DSFG signals in each mass and redshift bin using Websky simulations as explained above. We obtain zero false detections, which is consistent with a negligible systematic bias from dusty sources estimated above in Section 3.6. In a similar spirit, we also check the effect of random point sources in the maps. In this case, we inject point source signals with fluxes $S_{150} \in [0.5, 1, 2, 3]$ mJy, which are then scaled to other bands using a power-law relation with a spectral index $\alpha_{\rm dust} = 3.2$ and $\alpha_{\rm radio} = -0.6$ to represent DSFG and radio point source signals (George et al. 2015). Again, we do not see any false detections from DSGFs. This indicates that DSFGs do not show up as $\geqslant 5\sigma$ positive peaks in the Compton-y maps. For radio point sources, we find that the sources with flux $S_{150} \geqslant 2$ mJy can be potentially problematic. However, these radio point sources show up as negative peaks in the Compton-y maps and hence will not be classified as clusters.

4. Conclusion

We forecasted the number of galaxy clusters that can be detected using future CMB surveys, namely S4-Wide, S4-Ultra deep, and CMB-HD. Our forecasts used realistic simulations that include signals from galactic and extragalactic signals along with atmospheric and instrumental noise components. In the baseline footprint with $f_{\rm sky} = 50\%$, S4-Wide can detect close to 75,000 clusters, and the CMB-HD sample will contain three times more clusters. The smaller but deeper S4-Ultra deep survey can detect $\sim$14,000 clusters. Of these, 6000 (1500) will be at $z \geqslant 1.5$, and 1000 (350) clusters will be at $z \geqslant 2$ in the S4-Wide (S4-Ultra deep) cluster sample. The number of $z \geqslant 2$ clusters is an order of magnitude higher for the CMB-HD experiment. Including regions close to the galactic plane ($f_{\rm sky} = 17\%$) increases the sample size by roughly 20%.

The residual foreground signals, CIB in particular, dominate the small-scale variance in the Compton-y maps for CMB-S4. For CMB-HD, the variance from CIB is $\times 17$ lower at 150 GHz due to efficient subtraction of dusty galaxy sources (Sehgal et al. 2019). The CIB subtraction and a five-times-smaller beam are the reasons for a much larger cluster sample from CMB-HD. Given the importance of residual CIB signals and the tSZ $\times$ CIB correlation, we checked the systematic errors in the recovered cluster tSZ signals due to emission from galaxies within clusters. The effect of dusty star-forming galaxies was studied using Websky/MDPL2 simulations, while for radio galaxies, we use a simple constant flux model for all clusters. Our results indicate that systematic error due to the presence of dusty galaxies is much smaller than the statistical error $\leqslant 0.2\sigma$, but having a constant radio galaxy signal with $S_{150} = 0.5$ mJy

[14] https://mocks.cita.utoronto.ca/websky
[15] http://behroozi.users.hpc.arizona.edu/MDPL2/hlists/

can introduce $\sim 1\sigma$ bias. The models used for galactic foregrounds and RGs are basic and must be extended further. Nevertheless, the tests we performed to assess their contamination on the recovered tSZ signals are important for future SZ surveys.

We used a CMB-cluster lensing signal from both temperature and polarization to calibrate the cluster tSZ–mass scaling relation. We have ignored weak-lensing information from optical surveys in this work and note that including them can further improve the constraining power as well as act as an important systematic check for CMB-cluster lensing-based mass estimates. The internally calibrated cluster counts were combined with primary CMB (TT/EE/TE) spectra to derive cosmological constraints assuming a two-parameter extension to the standard model of cosmology ($\Lambda\mathrm{CDM} + \sum m_\nu + w_0$). We show that the constraints on the dark energy equation-of-state $\sigma(w_0)$ parameter can be between 1% and 2% for S4-Wide/S4-Ultra deep and sub-percent for CMB-HD. Similarly, the sum of neutrino masses $\sum m_\nu$ can detected at $\gtrsim 2.5\sigma$–4.5σ by both CMB-S4 and CMB-HD surveys assuming a normal hierarchy lower limit of 60 meV. We also assess the importance of combining cluster counts with primary CMB, significance of CMB-cluster lensing, choice of $\sigma(\tau_{\rm re})$ prior, effect of different redshift binning, and dependence of our result on the total survey time.

In addition to cosmology and scaling relation constraints, we also study the evolution of the ICM using two models. In the first case, we model cluster virialization in Equation (11) using the standard HSE bias parameter and a virialization efficiency parameter $\eta_{\rm v}$ that linearly scales with the tSZ signal from high redshift $z \geqslant 2$ clusters. We find $\sigma(\eta_{\rm v}) = 0.00471$, 0.0228, and 0.0339 from CMB-HD, S4-Wide, and S4-Ultra deep, respectively, indicating that the mean deviation in thermal energy of $z \geqslant 2$ clusters from their low redshift counterparts can be constrained to roughly 2%–4% by CMB-S4 and $<1\%$ by CMB-HD experiments. All three surveys can place sub-percent constraints on the HSE bias parameter. Our second model in Equation (13) is more physically motivated and calibrated using Omega500 hydrodynamical cosmological simulations. In this case, CMB-S4 can provide $\sim 4\%$ constraints on $B_{\rm v}$ and $\sim 33\%$ on $A_{\rm v}$, which controls the redshift evolution of the virialization mechanism. CMB-HD improves the constraining power by more than three times. This work represents a key step toward understanding the selection function of high redshift clusters and the evolution of the ICM using current and future CMB SZ surveys like AdvACT (Henderson et al. 2016), CMB-HD (Sehgal et al. 2019), CMB-S4 (CMB-S4 Collaboration 2019), SPT-3G (Benson et al. 2014; Bender et al. 2018), and SO (Ade et al. 2019). The binned cluster counts $N(z, M_L, q)$, Fisher matrices, and other associated products can be downloaded.[16]

We thank the entire CMB-S4 collaboration[17] for helpful comments and suggestions throughout the course of this work. We further thank Neelima Sehgal for feedback on the manuscript; Sebastian Bocquet and Nikhel Gupta for useful discussions; and Yuuki Omori for providing access to MDPL2 simulations. Finally, we thank the anonymous referee for the useful suggestions that helped in shaping this manuscript better. S.R. is supported by the Illinois Survey Science Fellowship from the Center for AstroPhysical Surveys at the National Center for Supercomputing Applications. S.R. and N. W. acknowledge support from NSF grants AST-1716965 and CSSI-1835865. S.R., N.W., G.H., and J.V. acknowledge support from NSF grant OPP-1852617. D.N. and H.A. acknowledge support from the facilities and staff of the Yale Center for Research Computing. N.B. acknowledges support from NSF grant AST-1910021. E.P. is supported by NASA grant 80NSSC18K0403 and the Simons Foundation award No. 615662, as well as NSF grant AST-1910678. C.R. acknowledges support from the Australian Research Council's Discovery Projects scheme (DP200101068). J.V. acknowledges support from NSF under grants AST-1715213 and AST-1716127. This work used computational and storage services associated with the Hoffman2 Shared Cluster provided by UCLA Institute for Digital Research and Education's Research Technology Group.

Appendix
A Physically Motivated Cluster Virialization Model

Galaxy clusters are dynamically active objects and generally out of HSE due to mergers and mass accretion processes. The lack of virialization is characterized by a nonthermal pressure fraction, $P_{\rm th}/P_{\rm tot}$, which quantifies the fraction of energy densities in unvirialized bulk and turbulent gas motions compared to the total pressure, $P_{\rm tot} = P_{\rm th} + P_{\rm nth}$ (e.g., Lau et al. 2009; Battaglia et al. 2012; Nelson et al. 2014a; Shi & Komatsu 2014; Yu et al. 2015). In the presence of the nonthermal pressure, the total pressure is given by the sum of the thermal and nonthermal pressure: $P_{\rm tot} = P_{\rm th} + P_{\rm nth}$, which in turn provides pressure support against gravitational collapse. Since the tSZ effect is sensitive to only the thermal pressure component $Y_{\rm tSZ} = Y_{\rm tot} - Y_{\rm nth}$, the observed integrated tSZ signal is reduced by

$$\frac{Y_{\rm nth}}{Y_{\rm tot}} = 1 - [\eta_{\rm v}(z)(1 - b_{\rm HSE})^{\alpha_Y}], \tag{A1}$$

which represents the combination of the lack of virialization and HSE mass bias from Equation (9), and Y is the integrated pressure of each component within the sphere of R_{500c} following Equation (6). Note that the nonthermal pressure is one of the dominant sources of systematic uncertainties in the HSE mass bias (e.g., Nagai et al. 2007b; Lau et al. 2013; Shi et al. 2016; Biffi et al. 2016; Angelinelli et al. 2020).

We compute the impact of the nonthermal pressure on the $Y_{\rm SZ} - M$ relation of high redshift clusters using the model presented in Green et al. (2020). First, we use the analytical model of Shi & Komatsu (2014) to compute the evolution of nonthermal pressure, by solving

$$\frac{d\sigma^2_{\rm nth}}{dt} = -\frac{\sigma^2_{\rm nth}}{t_{\rm dis}} + \eta\frac{d\sigma^2_{\rm tot}}{dt}, \tag{A2}$$

where $\sigma^2_{\rm nth} = P_{\rm nth}/\rho$ denotes the velocity dispersion due to nonthermal random motion, $t_{\rm dis}$ is the dissipation time of the turbulence scale $t_{\rm dis}$, $\sigma^2_{\rm tot} = P_{\rm tot}/\rho$ is the total velocity dispersion, and η is the fraction of energy accreted that is injected into turbulence motion. Due to the cosmic mass accretion process, the total velocity dispersion increases over time. The turbulence decays into thermal energy over the

[16] https://github.com/sriniraghunathan/tSZ_cluster_forecasts/
[17] https://people.cmb-s4.org/public/showdir.php

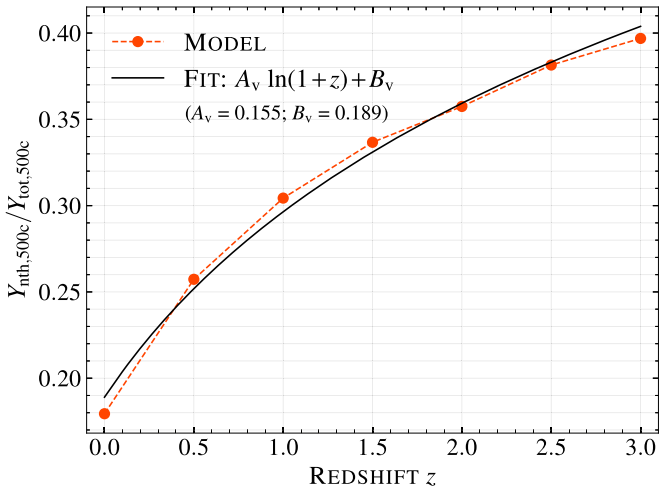

Figure A1. The ratio of the nonthermal pressure fraction, $Y_{\rm nth}/Y_{\rm tot}$, enclosed within the projected aperture radius of $R_{\rm 500c}$ for an $M_{\rm 500c} = 10^{14}\,M_\odot/h$ galaxy cluster as a function of redshift z. The model (orange) predicts that the nonthermal pressure increases as a function of redshift due to the enhanced mass accretion rate in the early universe. We propose a fitting function (black solid), Equation (A3), which describes the redshift evolution out to $z \approx 3$.

dissipation timescale $t_{\rm dis}$, which is proportional to the eddy turn-over time of the largest eddies, which is in turn proportional to the local orbital time, $t_{\rm dis}(r) = \beta t_{\rm orb}(r)/2$. The model has been calibrated using Omega500 hydrodynamical cosmological simulations (Nelson et al. 2014b), yielding the best-fit parameters of $\beta = 1$ and $\eta = 0.7$ (Shi et al. 2015). Given a cluster with mass $M_{\rm 500c}$, we generate the average mass accretion history $M(t)$ and concentration $c(t)$ of the cluster following van den Bosch et al. (2014) and Zhao et al. (2009), respectively. For the total pressure profiles, we use the KS01 (Komatsu & Seljak 2001) model, which is based on a polytropic gas in HSE with the NFW profile.

Figure A1 shows the fraction of the $Y(< R_{\rm 500c})$ signal in nonthermal pressure, $Y_{\rm nth}/Y_{\rm tot}$ as a function of redshift. For a constant mass $M_{\rm 500c} = 10^{14} M_\odot/h$, the model predicts that the fraction of the Y signal in nonthermal pressure can evolve from 20% at $z = 0$ to 40% at $z = 3$, indicating strong redshift dependence. The model predicts enhancement in the nonthermal pressure fraction toward high redshift due to the enhanced mass accretion rate in the early universe (Green et al. 2020). Our result suggests that the evolution of $Y_{\rm nth}/Y_{\rm tot}$ at $M_{\rm 500c} = 10^{14}\,M_\odot/h$ can be described by a simple function:

$$\frac{Y_{\rm nth}}{Y_{\rm tot}} = A_\nu \ln(1+z) + B_\nu, \qquad \text{(A3)}$$

where A_ν and B_ν are calibrated to 0.155 and 0.189.

ORCID iDs

Srinivasan Raghunathan https://orcid.org/0000-0003-1405-378X
Nathan Whitehorn https://orcid.org/0000-0002-3157-0407
Marcelo A. Alvarez https://orcid.org/0000-0002-2796-9650
Han Aung https://orcid.org/0000-0002-2153-6096
Nicholas Battaglia https://orcid.org/0000-0001-5846-0411
Gilbert P. Holder https://orcid.org/0000-0002-0463-6394
Daisuke Nagai https://orcid.org/0000-0002-6766-5942
Elena Pierpaoli https://orcid.org/0000-0002-7957-8993
Christian L. Reichardt https://orcid.org/0000-0003-2226-9169
Joaquin D. Vieira https://orcid.org/0000-0001-7192-3871

References

Ade, P., Aguirre, J., Ahmed, Z., et al. 2019, JCAP, 2019, 056
Alonso, D., Louis, T., Bull, P., & Ferreira, P. G. 2016, PhRvD, 94, 043522
Angelinelli, M., Vazza, F., Giocoli, C., et al. 2020, MNRAS, 495, 864
Arnaud, M., Pratt, G. W., Piffaretti, R., et al. 2010, A&A, 517, A92
Artis, E., Melin, J.-B., Bartlett, J. G., & Murray, C. 2021, A&A, 649, A47
Battaglia, N., Bond, J. R., Pfrommer, C., & Sievers, J. L. 2012, ApJ, 758, 74
Baxter, E. J., Keisler, R., Dodelson, S., et al. 2015, ApJ, 806, 247
Bender, A. N., Ade, P. A. R., Ahmed, Z., et al. 2018, Proc. SPIE, 10708, 1070803
Benson, B. A., Ade, P. A. R., Ahmed, Z., et al. 2014, Proc. SPIE, 9153, 91531P
Biffi, V., Borgani, S., Murante, G., et al. 2016, ApJ, 827, 112
Bleem, L. E., Stalder, B., de Haan, T., et al. 2015, ApJS, 216, 27
Bleem, L. E., Bocquet, S., Stalder, B., et al. 2020, ApJS, 247, 25
Bleem, L. E., Crawford, T. M., Ansarinejad, B., et al. 2022, ApJS, 258, 36
Bocquet, S., Dietrich, J. P., Schrabback, T., et al. 2019, ApJ, 878, 55
Cardoso, J.-F., Le Jeune, M., Delabrouille, J., Betoule, M., & Patanchon, G. 2008, ISTSP, 2, 735
Chluba, J., Nagai, D., Sazonov, S., & Nelson, K. 2012, MNRAS, 426, 510
CMB-S4 Collaboration 2019, arXiv:1907.04473
Cromer, D., Battaglia, N., & Madhavacheril, M. S. 2019, PhRvD, 100, 063529
Datta, R., Aiola, S., Choi, S. K., et al. 2019, MNRAS, 486, 5239
de Haan, T., Benson, B. A., Bleem, L. E., et al. 2016, ApJ, 832, 95
Delabrouille, J., Betoule, M., Melin, J. B., et al. 2013, A&A, 553, A96
Di Valentino, E., Brinckmann, T., Gerbino, M., et al. 2018, JCAP, 2018, 017
Everett, W. B., Zhang, L., Crawford, T. M., et al. 2020, ApJ, 900, 55
Fakhouri, O., Ma, C.-P., & Boylan-Kolchin, M. 2010, MNRAS, 406, 2267
Geach, J. E., & Peacock, J. A. 2017, NatAs, 1, 795
George, E. M., Reichardt, C. L., Aird, K. A., et al. 2015, ApJ, 799, 177
Green, D., Meyers, J., & van Engelen, A. 2017, JCAP, 2017, 005
Green, S. B., Aung, H., Nagai, D., & van den Bosch, F. C. 2020, MNRAS, 496, 2743
Gupta, N., Porciani, C., & Basu, K. 2020, arXiv:2003.09069
Gupta, N., Reichardt, C. L., Ade, P. A. R., et al. 2019, MNRAS, 490, 5712
Han, D., Sehgal, N., & Villaescusa-Navarro, F. 2021, PhRvD, 104, 123521
Hazra, D. K., Paoletti, D., Finelli, F., & Smoot, G. F. 2018, JCAP, 2018, 016
Henderson, S. W., Allison, R., Austermann, J., et al. 2016, JLTP, 184, 772
Hilton, M., Hasselfield, M., Sifón, C., et al. 2018, ApJS, 235, 20
Hilton, M., Sifón, C., Naess, S., et al. 2021, ApJS, 253, 3
Holder, G., Haiman, Z., & Mohr, J. J. 2001, ApJL, 560, L111
Holder, G. P., McCarthy, I. G., & Babul, A. 2007, MNRAS, 382, 1697
Hu, W., DeDeo, S., & Vale, C. 2007, NJPh, 9, 441
Huang, N., Bleem, L. E., Stalder, B., et al. 2020, AJ, 159, 110
Itoh, N., Kohyama, Y., & Nozawa, S. 1998, ApJ, 502, 7
Kaiser, N. 1986, MNRAS, 222, 323
Komatsu, E., & Seljak, U. 2001, MNRAS, 327, 1353
Lau, E. T., Kravtsov, A. V., & Nagai, D. 2009, ApJ, 705, 1129
Lau, E. T., Nagai, D., & Nelson, K. 2013, ApJ, 777, 151
Laureijs, R., Amiaux, J., Arduini, S., et al. 2011, arXiv:1110.3193
Lewis, A., Challinor, A., & Lasenby, A. 2000, ApJ, 538, 473
Lima, M., & Hu, W. 2004, PhRvD, 70, 043504
Louis, T., & Alonso, D. 2017, PhRvD, 95, 043517
LSST Science Collaboration, Abell, P. A., Allison, J., et al. 2009, arXiv:0912.0201
Madhavacheril, M., Sehgal, N., Allison, R., et al. 2015, PhRvL, 114, 151302
Madhavacheril, M. S., Battaglia, N., & Miyatake, H. 2017, PhRvD, 96, 103525
Madhavacheril, M. S., Hill, J. C., Næss, S., et al. 2020, PhRvD, 102, 023534
Mak, D. S. Y., & Pierpaoli, E. 2013, PhRvD, 87, 103518
Makiya, R., Hikage, C., & Komatsu, E. 2020, PASJ, 72, 26
Mantz, A., Allen, S. W., Ebeling, H., & Rapetti, D. 2008, MNRAS, 387, 1179
Mantz, A. B., Abdulla, Z., Carlstrom, J. E., et al. 2014, ApJ, 794, 157
Mantz, A. B., Abdulla, Z., Allen, S. W., et al. 2018, A&A, 620, A2
Melin, J.-B., & Bartlett, J. G. 2015, A&A, 578, A21
Melin, J. B., Bartlett, J. G., Cai, Z. Y., et al. 2018a, A&A, 617, A75
Melin, J. B., Bartlett, J. G., & Delabrouille, J. 2006, A&A, 459, 341
Melin, J. B., Bonaldi, A., Remazeilles, M., et al. 2018b, JCAP, 2018, 019
Merloni, A., Predehl, P., Becker, W., et al. 2012, arXiv:1209.3114
Mroczkowski, T., Nagai, D., Basu, K., et al. 2019, SSRv, 215, 17
Nagai, D., Kravtsov, A. V., & Vikhlinin, A. 2007a, ApJ, 668, 1

Nagai, D., Vikhlinin, A., & Kravtsov, A. V. 2007b, ApJ, 655, 98
Navarro, J. F., Frenk, C. S., & White, S. D. M. 1996, ApJ, 462, 563
Nelson, K., Lau, E. T., & Nagai, D. 2014a, ApJ, 792, 25
Nelson, K., Lau, E. T., Nagai, D., Rudd, D. H., & Yu, L. 2014b, ApJ, 782, 107
Planck Collaboration, Ade, P. A. R., Aghanim, N., et al. 2014, A&A, 571, A12
Planck Collaboration, Ade, P. A. R., Aghanim, N., et al. 2016a, A&A, 594, A27
Planck Collaboration, Ade, P. A. R., Aghanim, N., et al. 2016b, A&A, 594, A24
Planck Collaboration, Ade, P. A. R., Aghanim, N., et al. 2016c, A&A, 594, A13
Planck Collaboration, Adam, R., Ade, P. A. R., et al. 2016d, A&A, 596, A104
Planck Collaboration, Ade, P. A. R., Aghanim, N., et al. 2016e, A&A, 594, A23
Planck Collaboration, Aghanim, N., Akrami, Y., et al. 2020a, A&A, 641, A6
Planck Collaboration, Akrami, Y., Ashdown, M., et al. 2020b, A&A, 641, A11
Popesso, P., Biviano, A., Finoguenov, A., et al. 2015, A&A, 579, A132
Raghunathan, S., Holder, G. P., Bartlett, J. G., et al. 2019a, JCAP, 2019, 037
Raghunathan, S., Patil, S., Baxter, E., et al. 2019b, PhRvL, 123, 181301
Raghunathan, S., Patil, S., Baxter, E. J., et al. 2017, JCAP, 8, 030
Reichardt, C. L., Patil, S., Ade, P. A. R., et al. 2021, ApJ, 908, 199
Remazeilles, M., Delabrouille, J., & Cardoso, J.-F. 2011, MNRAS, 410, 2481
Rozo, E., Wechsler, R. H., Rykoff, E. S., et al. 2010, ApJ, 708, 645
Salvati, L., Douspis, M., & Aghanim, N. 2018, A&A, 614, A13
Sartoris, B., Borgani, S., Rosati, P., & Weller, J. 2012, MNRAS, 423, 2503
Sehgal, N., Aiola, S., Akrami, Y., et al. 2019, BAAS, 51, 6
Sehgal, N., Aiola, S., Akrami, Y., et al. 2020, arXiv:2002.12714
Shi, X., & Komatsu, E. 2014, MNRAS, 442, 521
Shi, X., Komatsu, E., Nagai, D., & Lau, E. T. 2016, MNRAS, 455, 2936
Shi, X., Komatsu, E., Nelson, K., & Nagai, D. 2015, MNRAS, 448, 1020
Stein, G., Alvarez, M. A., Bond, J. R., van Engelen, A., & Battaglia, N. 2020, JCAP, 2020, 012
Sunyaev, R. A., & Zel'dovich, Y. B. 1970, CoASP, 2, 66
Tegmark, M. 1997, PhRvD, 56, 4514
Thorne, B., Dunkley, J., Alonso, D., & Næss, S. 2017, MNRAS, 469, 2821
Tinker, J., Kravtsov, A. V., Klypin, A., et al. 2008, ApJ, 688, 709
van den Bosch, F. C., Jiang, F., Hearin, A., et al. 2014, MNRAS, 445, 1713
Viero, M. P., Reichardt, C. L., Benson, B. A., et al. 2019, ApJ, 881, 96
Vikhlinin, A., Kravtsov, A. V., Burenin, R. A., et al. 2009, ApJ, 692, 1060
von der Linden, A., Allen, M. T., Applegate, D. E., et al. 2014, MNRAS, 439, 2
Yu, L., Nelson, K., & Nagai, D. 2015, ApJ, 807, 12
Zhao, D. H., Jing, Y. P., Mo, H. J., & Börner, G. 2009, ApJ, 707, 354
Zhao, H. 1996, MNRAS, 278, 488
Zubeldia, Í., & Challinor, A. 2019, MNRAS, 489, 401